Received: 20 October 2021 | Revised: 4 May 2022 | Accepted: 20 May 2022

DOI: 10.1111/gbi.12506

ORIGINAL ARTICLE

gebiology WILEY

# Distinguishing cellular from abiotic spheroidal microstructures in the ca. 3.4 Ga Strelley Pool Formation

**Maxime Coutant**[1,2] | **Kevin Lepot**[1,3] | **Alexandre Fadel**[4] | **Ahmed Addad**[4] | **Elodie Richard**[5] | **David Troadec**[6] | **Sandra Ventalon**[1] | **Kenichiro Sugitani**[7] | **Emmanuelle J. Javaux**[2]

[1]Univ. Lille, CNRS, Univ. Littoral Côte d'Opale, UMR 8187, LOG – Laboratoire d'Océanologie et de Géosciences, Lille, France

[2]Early Life Traces & Evolution-Astrobiology, UR Astrobiology, University of Liège, Liège, Belgium

[3]Institut Universitaire de France (IUF), France

[4]UMR 8207 – UMET – Unité Matériaux et Transformations, Univ. Lille, CNRS, INRAE, Centrale Lille, Lille, France

[5]Univ. Lille, CNRS, INSERM, CHU Lille, Institut Pasteur de Lille, US 41 – UAR 2014 – PLBS, Lille, France

[6]Univ. Lille, CNRS, Centrale Lille, Junia, Univ. Polytechnique Hauts-de-France, UMR 8520 – IEMN – Institut d'Electronique de Microélectronique et de Nanotechnologie, Lille, France

[7]Graduate School of Environmental Studies, Nagoya University, Nagoya, Japan

**Correspondence**
Maxime Coutant, UMR 8187 – LOG – Laboratoire d'Océanologie et de Géosciences, Univ. Lille, CNRS, Univ. Littoral Côte d'Opale, Lille, France.
Email: maxime.coutant@uliege.be

**Funding information**
Financial support for this project was provided by the Agence Nationale de la Recherche, France (ANR M6fossils: ANR-15-CE31-0003-01 to K.L.), and Région Hauts de France (project Vison-AIRR iM4 to K.L.). Preliminary analyses were carried using financial support of FRS-FNRS FRFC Grant no. 2.4558.09F (E.J.J.), CNRS-INSU (Program INTERRVIE – K.L.) and FNRS (K.L.). Support also comes from ULiege-UR Astrobiology (M.C. scholarship), M.C. is a FRIA grantee of the Fonds de la Recherche Scientifique – FNRS and FNRS

## Abstract

The morphogenesis of most carbonaceous microstructures that resemble microfossils in Archean (4–2.5 Ga old) rocks remains debated. The associated carbonaceous matter may even—in some cases—derive from abiotic organic molecules. Mineral growths associated with organic matter migration may mimic microbial cells, some anatomical features, and known microfossils—in particular those with simple spheroid shapes. Here, spheroid microstructures from a chert of the ca. 3.4 Ga Strelley Pool Formation (SPF) of the Pilbara Craton (Western Australia) were imaged and analyzed with a combination of high-resolution in situ techniques. This provides new insights into carbonaceous matter distributions and their relationships with the crystallographic textures of associated quartz. Thus, we describe five new types of spheroids and discuss their morphogenesis. In at least three types of microstructures, wall coalescence argues for migration of carbonaceous matter onto abiotic siliceous spherulites or diffusion in poorly crystalline silica. The nanoparticulate walls of these coalescent structures often cut across multiple quartz crystals, consistent with migration in/on silica prior to quartz recrystallization. Sub-continuous walls lying at quartz boundaries occur in some coalescent vesicles. This weakens the "continuous carbonaceous wall" criterion proposed to support cellular inferences. In contrast, some clustered spheroids display wrinkled sub-continuous double walls, and a large sphere shows a thick sub-continuous wall with pustules and depressions. These features appear consistent with *post-mortem* cell alteration, although abiotic morphogenesis remains difficult to rule out. We compared these siliceous and carbonaceous microstructures to coalescent pyritic spheroids from the same sample, which likely formed as "colloidal" structures in hydrothermal context. The pyrites display a smaller size and only limited carbonaceous coatings, arguing that they could not have acted as precursors to siliceous spheroids. This study revealed new textural features arguing for abiotic morphogenesis of some Archean spheroids. The absence of these features in distinct types of spheroids leaves open the microfossil hypothesis in the same rock. Distinction of such characteristics could help addressing further the origin of other candidate microfossils. This study calls for similar investigations of metamorphosed microfossiliferous rocks and

PDR 35284099 “Life in coastal Archean Environments” (E.J.J). The authors thank x anonymous reviewers for their constructive comments.

of the products of in vitro growth of cell-mimicking structures in presence of organics and silica.

**KEYWORDS**
Archean, biomorphs, microfossils, spheroids, Strelley Pool Formation

## 1 | INTRODUCTION

Due to their simple shape, various types of Archean spherical and filamentous carbonaceous microstructures have commonly been regarded as dubiofossils or discarded as non-fossils as they could have formed during accretion and/or displacement of carbonaceous matter associated with growth of mineral templates (Brasier et al., 2005; Buick, 1990; Lepot, 2020; McMahon & Cosmidis, 2021). Dubiofossils formed in early Archean volcanoclastic rocks as volcanic vesicles became covered by carbonaceous matter (Hickman-Lewis, Cavalazzi, Foucher, & Westall, 2018; Wacey, Noffke, Saunders, Guagliardo, & Pyle, 2018a; Wacey, Saunders, & Kong, 2018b). Various spheroid and filamentous biomorphs can also self-assemble by mixture of (pre)biotic organic compounds in ambient or hydrothermal conditions, and self-assembly of organic-mineral structures (Cosmidis & Templeton, 2016; Fox & Yuyama, 1963; McMahon & Cosmidis, 2021; Nims, Lafond, Alleon, Templeton, & Cosmidis, 2021; Rouillard, Van Zuilen, Pisapia, & Garcia-Ruiz, 2021). Thus spherical microstructures have to be considered carefully to avoid misinterpretation as microfossils (Javaux, 2019; Lepot, 2020; McMahon & Cosmidis, 2021; Rouillard et al., 2021).

The ca. 3.4 Ga Strelley Pool Formation (SPF) of the East Terrane of the Pilbara Craton (Western Australia) displays diverse stromatolitic deposits. The biogenicity of its carbonate stromatolites has been argued based on sedimentological and morphological studies (Allwood, Walter, Kamber, Marshall, & Burch, 2006), and some siliceous stromatolites preserving organic laminae also likely have a biogenic origin (Lepot, 2020; Sugitani et al., 2015a). The SPF, including stromatolitic and non-stromatolitic black cherts as well as quartz-cemented sandstones yielded a suite of carbonaceous microstructures that comprises spheroids, filaments, and lenses. They have all been considered as candidates for the oldest microfossils (Delarue et al., 2020; Lepot et al., 2013; Oehler, Walsh, Sugitani, Liu, & House, 2017; Schopf, 2006; Schopf et al., 2017; Sugitani et al., 2010, 2015a; Wacey et al., 2012; Wacey, Kilburn, Saunders, Cliff, & Brasier, 2011). Early Archean chert from the Barberton Greenstone Belt of South Africa displayed quite similar assemblage of microstructures (Engel et al., 1968; Glikson et al., 2008; Pflug, 1967; Schopf, 1976; Walsh, 1992).

The SPF rocks experienced synsedimentary hydrothermal fluids (Sugitani et al., 2015b) and organic matter maturation equivalent to ca. 300–350°C metamorphism (Lepot et al., 2013). Nevertheless, organic matter displays functionalized polycyclic aromatics (Marshall et al., 2007), as well as heteroatoms (O, N and P) (Alleon et al., 2018; Delarue et al., 2020; Oehler et al., 2010). However, abiotic carbonaceous matter can be formed in such hydrothermally-influenced environments (Brasier et al., 2002; McCollom & Seewald, 2006) that may bear heteroatomic functional groups (Lepot, 2020), increasing the challenge of assessing biogenicity. Contaminations by younger endolithic microbes (Westall & Folk, 2003) or migrated oil must also be evaluated. For instance, a recent study proposed that anatomically shaped cavities left by the 1.9 Ga Gunflint microfossils may have been filled with oil (Rasmussen, Muhling, & Fischer, 2021). Microscale isotope ratio analyses distinguished $\delta^{13}$C of fossil-like microstructures and those of carbonaceous clots and veins of the SPF (Lepot et al., 2013). These texture-correlated C-isotope compositions, and the similar C-isotope compositions recorded in fossil-like structures of the ca. 3.0 Ga Farrel Quartzite of Western Australia (House, Oehler, Sugitani, & Mimura, 2013; Oehler et al., 2017) argue against an all-abiotic hydrothermal origin for the organic matter in these rocks and support the microfossil interpretation, although the possibility of multiple generations of fluid circulation has been suggested (Wacey et al., 2018a).

Cell-wall folding, as observed in the spheroidal microfossils of the 3.22 Ga Moodies Group of South Africa (Javaux, Marshall, & Bekker, 2010) and the ca. 3.0 Ga Farrel Quartzite (Sugitani, Grey, Nagaoka, & Mimura, 2009a; and Javaux, personal observations), has so far not been clearly demonstrated in spheroids of the SPF. Inner bodies, as observed in the large spheroids of the Farrel Quartzite (Sugitani, Grey, Nagaoka, Mimura, & Walter, 2009b), appear absent in SPF spheroids. Ultrastructure of SPF spheroids was investigated at the sub-micrometric scale in cements of SPF sandstones using focus ion beam (FIB) sectioning coupled to SEM or to Scanning Transmitted Electron Microscopy (STEM) and Energy Filtered Transmitted Electron Microscopy (EFTEM) (Wacey et al., 2011, 2012). This yielded an in situ cross-sectional view that resolved carbonaceous textures in their host quartz matrix at the nanoscale. Some SPF spheroids thus displayed cross-sections with sub-continuous carbonaceous walls lying at the boundaries of quartz grains, a texture that resembles that of microfossils of the ca. 1.9 Ga Gunflint chert (Brasier, Antcliffe, Saunders, & Wacey, 2015; Wacey et al., 2012). In contrast, other spheroids of these sandstones displayed diffuse walls of sub-micrometric carbonaceous particles, which have been interpreted as abiotic textures (Wacey et al., 2012). The textural relationship between quartz structures and these particulate carbonaceous spheroids has not yet been elucidated because grain boundaries are not observed in SEM images. Moreover, a destructive method that consists in sequential FIB ablation alternated with SEM image acquisition (FIB-SEM) enabled 3D reconstruction of a spheroid (Brasier et al., 2015; Wacey et al., 2012). Confocal laser scanning microscopy (CLSM) can also perform 3D imaging without destruction of specimens in thin sections (Schopf, Tripathi, & Kudryavtsev, 2006).

Acid maceration released various types of spheroids from SPF cherts, including hollow specimens with discontinuous surfaces ~10 μm across, alveolar specimens ~10 μm across, globular specimens >10 μm across, and smooth, continuously walled specimens >10 μm across (Delarue et al., 2020). Thus far, it remains difficult to link the observations on macerated spheroids to those observed in these sections, possibly because some spheroids (e.g., the nanoparticulate) may disintegrate during maceration. Other spheroids collapse when extracted and are difficult to relate to their original 3D shape, and possibly due to unresolved diversity sampled and observed in thin sections compared to large sample volumes used for maceration. In our view, 3D imaging as performed in Wacey et al. (2012) link the subcontinuous walls observed in thin sections to the discontinuous surfaces of the hollow macerated specimens of Delarue et al. (2020). The small (~10 μm) irregularly walled spheres where the wall is thick enough to appear in SEM in Lepot et al. (2013) likely belong to the same type.

Here, we studied the larger (>10 μm) spheroids in SPF samples and searched for new criteria to assess their cellular or abiotic morphogenesis at the micro- and nanoscales. Five thin sections from the sample WF4 (Lepot et al., 2013; Sugitani et al., 2010) yielded more than 70 specimens of previously undescribed carbonaceous spheroids. We performed a complete morphological and structural analysis of carbonaceous wall structures in these spheroids using a combination of transmitted-light microscopy and CLSM. This allowed us to perform 3D reconstruction and virtual cutting, which is particularly useful when microstructures appear opaque due to their dark carbonaceous contents. Electron backscattered diffraction (EBSD) was used to document quartz crystal structures cropping out at the surface of thin sections. Preparation of ultrathin sections with FIB permitted nano-scale analysis of carbonaceous textures and mineral matrix petrography using STEM as well as nano-diffraction mapping. This leads us to distinguish five types of spheroids, among which two types derive from complete abiotic morphogenesis, a dubiofossil type with abiotic internal vesicles and two other types of dubiofossils. Pyritic spheroids were also documented and compared to the carbonaceous spheroids.

## 2 | GEOLOGICAL SETTING AND SAMPLE LOCALITY

The ca. 3.4 Ga SPF is a constituent of the Pilbara Craton (Van Kranendonk, 2006), part of the Pilbara Supergroup, which comprises 11 greenstone belts. This formation is bounded by the ca. 3520–3427 Ma Warrawoona Group dominated by mafic volcanic rocks with minor felsic volcanics, and the ca. 3350–3315 Ma Kelly Group that displays mainly basaltic and ultramafic lavas. The SPF was previously related to the Kelly Group, but has been independently positioned and is overlain by the Euro Basalt from the Kelly Group. Up to 1000 m thick, the SPF is composed of siliciclastic conglomerates and sandstones, dolomitic stromatolites, and black and grey-to-white cherts that are either primary or derived from silicified carbonates. The WF4 sample (5 thin sections prepared serially as parallel cuttings of the same piece of rock) studied here was firstly described in Sugitani et al. (2010) and studied in Lepot et al. (2013). This sample comes from a massive black chert from the informally named "Waterfall locality" (20°20,039″S, 119°25,009″E) in the Goldsworthy greenstone belt, where a 60 m thick outcrop of coarse sandstone interbedded with 1–3 m thick chert units is uncomformably overlain by the Euro Basalt (Sugitani et al., 2010). Chert beds display black-to-grey laminae within a light-to-white silica matrix. Sedimentological context, trace element patterns and metal abundances, and petrography suggest that the cherts deposited in a coastal hydrothermal field (Sugitani et al., 2015b). Shallow water deposition is supported by pseudomorphs after evaporite minerals and close association of the massive black cherts with laminated black cherts displaying conical and domical structures that trap sand grains and that are interpreted as stromatolites (Sugitani et al., 2015b). This is consistent with a shallow-marine, tidal and supratidal environment of deposit inferred from the study of other localities (Van Kranendonk, 2006).

## 3 | METHODS

### 3.1 | Optical microscopy

Five thin sections were observed under optical microscope with transmitted polarized and non-polarized and non-analyzed light as well as reflected light using a Nikon Eclipse Ni-E with automatized stage (at LOG, U.Lille). We used five Nikon TU plan fluor objectives: 5X NA0.10, 10X NA0.30, 20X NA0.45, 50X NA0.80, and 100X NA0.90, a Nikon DS-Ri2 camera, and the NIS Elements AR 5.02.00 software. We acquired Z-stacks of multiple images collected at evenly-spaced focal depths. Unless otherwise specified, single focal plane images are shown. Z-stack were sometimes assembled using extended depth focus, which overlays the in-focus zones of each Z image (discarding the rest) to form a single, "multiplane" image where all zones appear in focus. When carbonaceous structures were too opaque, we also recorded images using various exposure time and combined these images using the high dynamic range method to produce images with no under/over exposure. Mosaics were also created displaying a whole view of the sections (Figures S1a-e). Optical microscopy in Figures 6a-b and Figure S16a-c was performed using an Olympus BX50 microscope (at Early Life Traces & Evolution-Astrobiology, U.Liege) using a x100 oil-immersion objective.

### 3.2 | Scanning electron microscopy and electron backscattered diffraction

For Figure S2, BSE images and EDX spectra and mappings of a gold-coated thin section were acquired with a Hitachi S3400 SEM (at LOG, U.Lille) operated at 10 kV and 10 mm working distance.

Grain boundaries of quartz are difficult to distinguish in petrographic thin section when grains are much thinner that the section. To distinguish quartz crystals in SEM, we performed EBSD on uncoated polished thin sections with a Hitachi SU 5000 field-emission SEM (at UW-Madison) fitted with Symmetry/Oxford Instruments EBSD system and operated at 20 kV, in low vacuum mode (10 Pa). The EBSD scan were performed at approximately 200 points per second with a step size ranging between 300 and 500 nm. The EBSD patterns were indexed using 9–10 Kikuchi bands based on the database of $\alpha$ –quartz crystallographic orientation patterns from Kim-Zajonz, Werner, and Schulz (1999). No post-processing was performed on the obtained map. The EBSD band contrast images reflect the pattern quality/intensity of the Kikuchi bands through Hough transformation. Because the pattern quality becomes lower at the grain boundaries due to overlapping patterns, the microstructure of the quartz can be observed with the band contrast images (which also display defects such as polishing holes, scratches, …). Finally, sets of three Inverse Pole Figure (IPF) images permit visualization the orientation of the quartz crystals with respect to each of the normal directions, X, Y, and Z. In IPF images, Euler angles of crystals with respect to X, Y, and Z are shown using the rainbow scale using the IPF color key shown in Figure S3d. Single crystals are thus inferred for given areas displaying a homogenous color along the three axes and the absence of internal grain boundaries. As maps were acquired with the sample tilted with respect to both the electron source and the EBSD camera, angular image distortion appeared. This was corrected with a trapezoid deformation to correspond to images recorded on horizontal thin sections.

## 3.3 | Confocal laser scanning microscopy

Carbonaceous microstructures were analyzed with a Zeiss LSM 780 (Carl Zeiss) confocal head associated with a Z1 Zeiss observer microscope (at UMS PLBS BiCeL CS, U.Lille). We used a Plan-Apochromat 40×/1.3 Oil DIC M27 objective (Zeiss) under oil immersion, 488 nm laser excitation, and collected the complete signal between 497 and 685 nm. A glass coverslip, held with a drop of water, was used to separate some sections (later used for FIB-TEM) from the oil-immersion medium. For Z stack acquisitions, automated Z-brightness adjustment was used to compensate variations in signal with depth in the quartz matrix. Single focal planes, 3D reconstructions, and virtual vertical slices were obtained using the Zen 2 (black edition) software by Carl Zeiss.

## 3.4 | Focus ion beam

Ultrathin (ca. 100–200 nm) sections were cut through various carbonaceous microstructures close to the surface of petrographic thin sections using a FEI Dual Beam Strata 235 FIB (at IEMN, U.Lille), and one FIB section (Figure 6) using a FEI Helios 600 NanoLab Dual Beam FIB (at CP2M, U.Lille). In brief, after deposition of a protective micrometric strip of Pt onto the gold-coated petrographic sections, a Ga ion beam was used to etch the samples. The resulting sections were attached onto a copper TEM grid using in situ micromanipulation and Pt-welding and further etched with decreasing ion currents.

## 3.5 | Transmission electron microscopy

An FEI Titan$^3$ (at the electron microscopy facility of the Advanced Characterization Platform of the Chevreul Institute, U.Lille) operated at 300 kV was used to record STEM-HAADF (high-angle annular dark field), dark-field STEM, EDX maps and spectra, as well as energy-filtered maps of carbon. Energy-filtered maps of carbon were recorded in TEM mode using a 2048x2048 pixel detector (by Gatan) using the three-window method. Energy-filtered images allow distinction of carbonaceous matter from low-density areas such as pores, which is not possible in dark-field STEM. Mosaics of EFTEM images (Figures 3c, 5e, 7e, 10b, Figures S11, S12) were assembled manually after contrast-brightness adjustments on individual images. Contrast-brightness heterogeneities appear between the different parts of the mosaics due to the differences in grey-level ranges assigned during acquisition and have been corrected partly (in Figures 3c, 7e and Figure S11b) with contrast-brightness adjustments on individual parts, before homogenous gamma correction (applied to all mosaics); in this case mosaics with homogenous contrast-brightness adjustments are also annexed. For Figure 6, a FEI Tecnai G2 20 (at the electron microscopy facility of the Advanced Characterization Platform of the Chevreul Institute, U.Lille) operated at 200 kV was used to record pseudo-HAADF STEM images (i.e., dark-field images recorded at high angles using an off-axis detector) and dark-field TEM images (associated selected area electron diffractions shown in Figure S10). The dark-field STEM image of Figure 6d and EDX elemental maps of Figure 6i, k and m were recorded using a CM30 STEM (at the electron microscopy facility of the Advanced Characterization Platform of the Chevreul Institute, U.Lille) operated at 300 kV with probe size smaller than 13 nm.

Nano-diffraction mappings were acquired using the ASTAR™ system from NanoMEGAS (Forest, Belgium) to document relationships between carbonaceous textures and those of the associated micro/nano quartz crystals. For this, we used the Tecnai G20 instrument operated at 200 kV (at the electron microscopy facility of the Advanced Characterization Platform of the Chevreul Institute, U.Lille) with a convergent electron beam allowing diffraction on nanometric spots (spot size 7) with a precession rotation. The diffraction patterns are then re-aligned along the vertical axis using a descan magnetic lens, thus gathering all diffraction patterns generated at a camera length of 10.5 cm. The electron beam sweeps the FIB section in the horizontal plane to build a complete map of diffraction patterns. Diffraction maps were processed using DiffGen/Index (NanoMEGAS software) after building a database of all possible nano-diffraction patterns using published quartz crystal lattice

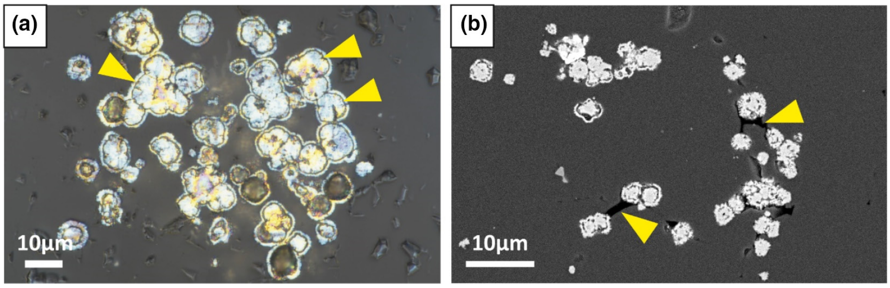

FIGURE 1 Pyrite spheroids. Sample WF4-1 (a) and WF4' (b). (a) Reflected-light photomicrograph of a cluster of pyrite spheroid, indicating a crown inside the pyrites spheres. (b) SEM BSE image of pyrites spheres (see Figure S2c for EDX spectra), yellow arrowheads show carbonaceous bridges between pyrite spheres

parameters (Kim-Zajonz et al., 1999). Thus, to help indexing diffraction images, we corrected all diffraction images by using a fuzzy mask (reducing locally the brightness of the central spot) and set the maximum polar image radius to 50–60. Camera length and distortion of the images corrected to improve fitting of the observed patterns. Then the recognition was used in full-matching setting, using automatic refinement to gently replace the center of the pattern (in case of smooth image off-centering), through 100 iterations at each pixel analyzed. Thus, the software fitted the data with the simulated diffraction patterns to obtain the orientations of quartz crystals at every pixel of the maps. These orientations are given as Euler angles. The differences in orientation between the quartz crystals are then represented by different colors using a rainbow color scale where similar orientations will show similar colors and small misorientations will show up as neighboring colors on the rainbow scale where each crystallographic direction [100], [010], [001] is associated to an RGB gradient. In addition, "grain boundary" maps were generated with the Map Viewer (NanoMEGAS) software, which also display other features such as crystal defects. The overlay and/or comparison of Euler angle maps and grain boundary maps allowed us to outline single-quartz crystals.

### 3.6 | Scanning transmission X-ray microscopy

The map of aromatic carbon shown in Figure 6e was recorded using the experimental setup detailed in (Lepot et al., 2017), at the Canadian Light Source synchrotron beamline 10ID-1 (SM beamline). This map was produced by subtracting single X-ray absorption images recorded in "mapstack" mode at 285.3 (maximum absorption of aromatic C) and 275 eV (pre-edge absorption background).

## 4 | RESULTS

### 4.1 | General composition of the cherts

The observed samples are composed of a quartz matrix with pure quartz and quartz+carbonaceous veins, punctuated with carbonaceous clot structures and diverse opaque minerals (Figures S1). Quartz crystals are mostly micrometric to sub-micrometric (~0.5–5 µm) with equant to sub-equant shapes, as detailed below.

Opaque minerals and their weathering products are mostly found associated with organic-rich zones (Figure S1). These include zones rich in stellate sphalerites (Sugitani et al., 2015b). Other sulfides distributed throughout the carbonaceous zones of the thin sections are dominated by spherulitic pyrites displaying diameters of ca. ~2 to 9 µm, coalescence patterns, and carbonaceous bridges and/or inclusions (Figure 1 and Figure S2). Phyllosilicates, likely Mg-Chlorite, sometimes cross-cut the pyrite spheres (Figure S2b). Sulfides of As-Ni (likely Gersdorffite) and Cu (covellite or chalcocite) also occur within spherulitic pyrite clusters (Figures S2).

Multi-millimetric zones of the WF4 sections display white (organic-poor) botryoidal quartz (Figure S1) that hosts filamentous carbonaceous matter (Lepot, 2020). Carbonaceous veins occur in WF4 (Lepot et al., 2013) in addition to late pure-quartz veins (Figure S1). The samples display carbonaceous films, carbonaceous clots, lenticular microstructures, and clusters of spheres ca. 10 µm or less in diameter, with granular and discontinuous walls as previously described that were interpreted as microfossils (Figure S1b-3, Lepot et al., 2013; Sugitani et al., 2010; Sugitani et al., 2015a). These smaller spheres (Figure S1b-3-5) are not further documented in this study where we report on new, distinct spheroids larger than 10 µm. The quartz matrix that hosts these carbonaceous microstructures displays a finely reticulated carbonaceous stain that forms clots within pure quartz areas (Figure S1).

### 4.2 | Unusual carbon-quartz spheroidal microstructures

In addition to the previously described lenticular microstructures and smaller (≤10 µm) spheres, thin sections of WF4 delivered more than 70 specimens of unusual, carbonaceous spheroids ~15 to more than 100 µm in diameter. We classify in the next sections these larger spheroids under five different types based on their morphologies as observed under the optical microscope.

Types 1 to 3 represent the most abundant microstructures observed while Type 4 and Type 5 specimens are scarce. Types 1 to 3 microspheres are not spread throughout the thin sections (unlike lenticular microstructures), but they mostly occur in close association with a thick, contorted and irregular carbonaceous layer (Figure S1). Most of these spheroids are surrounded by a fluffy network of nano-particulate carbonaceous matter of variable spatial extent (e.g., Figure 2a, b).

### 4.2.1 | Type 1 spheroids

Type 1 spheroids comprise specimens that display multi-micrometric internal carbonaceous masses and a single wall (Figure 2a, b). These spheroids range between ca. 15 to 50 µm in diameter. They generally display a single smooth, hyaline wall under the optical microscope (Figure 2a), although some display a granular wall (Figure 2b). They are essentially filled with quartz (Figure 2c, d, Figure S3). Type 1 spheroids appear as individuals (Figure 2a) or as coalescent clusters of hemispheres (Figure 2b, Figures S4 and S5). Unusual microstructures that share the two main features (internal masses and single wall) of Type 1, but with a global shape that significantly deviates from spherical, are also classified here in Type 1 (Figures S5 and S6).

Electron Back-Scattered Diffraction (Figures 2c-d, Figures S3–S6) shows that quartz crystals within Type 1 spheroids are generally coarser than those that occur in/around their carbonaceous wall and those occurring in the surrounding carbonaceous-rich nanoparticulate network. The white quartz matrix that is poor in carbonaceous matter displays quartz crystal sizes similar or slightly smaller than those in the spheroids. EBSD also revealed that the nanoparticulate carbonaceous matter in parts of the walls of these spheroids is locally included in coarser quartz crystals that display cross-cutting relationships with the walls (yellow arrowheads in Figure 2a).

The FIB-sectioned specimen was of coalescent spheroids. It displays both nanoparticulate (~10 nm in diameter) carbonaceous matter embedded in quartz crystals as well as carbonaceous films lying at grain boundaries (Figure 3). Micrometric quartz crystals in this outer zone are generally free of carbonaceous inclusions. In contrast, the walls of coalescent spheroids mostly comprise bands speckled with nanoparticles. High-resolution diffraction mapping confirm that organic matter is lying either at quartz crystals boundaries (orange-dashed line in Figure 3) or occurring as bands composed of nano-inclusions, which cross-cut quartz crystals (blue-dashed lines in Figure 3). Crystals do not display a preferential orientation (Figure S7). The carbonaceous masses within the spheroids display a geometric shape sculpted by the equant faces of surrounding micro-quartz (Figures 2-3). Nanocrystals of sulfides of Fe + Ni as well as oxides of Fe + Sb and of Cr (+Ti, Fe, Zn) occur embedded with carbonaceous nanoparticles in spheroid walls (Figures 3e-f).

### 4.2.2 | Type 2 spheroids

Type 2 is the most complex type to define according to its multiple textural characteristics, many of which are shared with other types. It comprises spheroids of similar size as Type 1, but that display one to five internal vesicles (Figure 4) instead of irregular carbonaceous

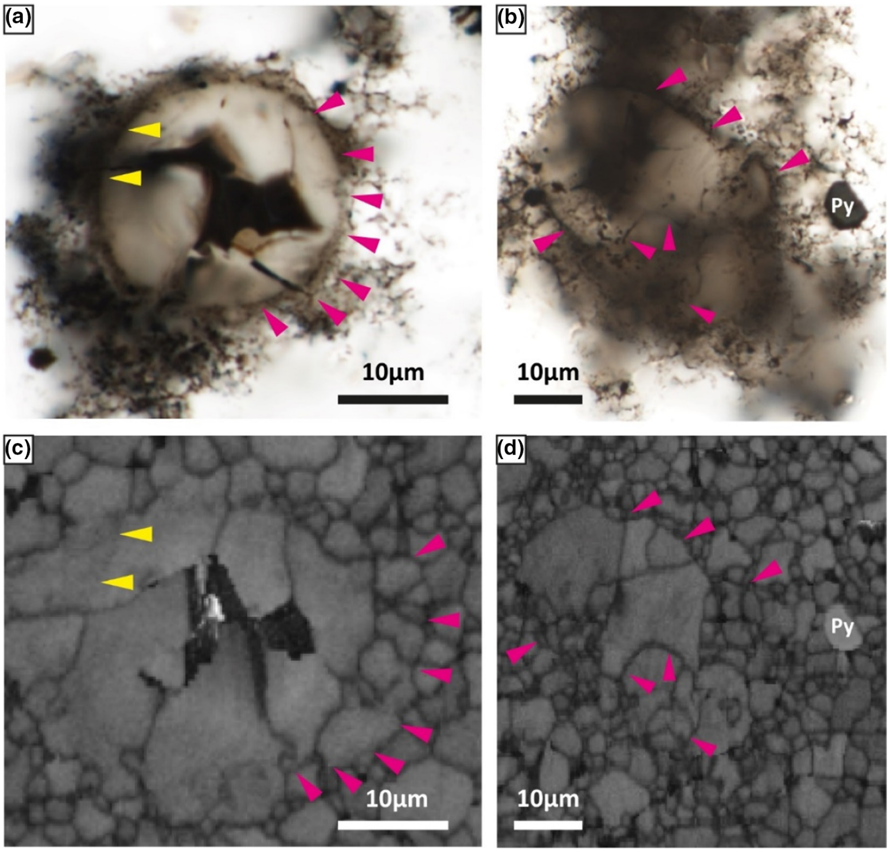

FIGURE 2 Type-1 spheroids. Sample WF4-1. (a-b): photomicrographs, c-d: Scanning electron microscopy–Electron backscattered diffraction (SEM-EBSD). (a) Spheroid displaying a dark carbonaceous core and a smooth and hyaline wall (arrowheads). (b) This specimen displays coalescence of multiple hemispheres. Note pyrite (Py) in the surrounding carbonaceous network. (c, d) SEM-EBSD band contrast images of the zones in a and b, respectively, showing quartz crystal boundaries. Yellow arrowheads highlight the parts of carbonaceous walls that are embedded in quartz, whereas pink arrows indicate the location of outer wall (in a-c) and inner-vesicle walls (in b-d) where carbonaceous matter lies at grain boundaries

masses. The outer wall is usually single and granular (Figure 4), although a thin second wall appears in the specimen of Figure 4a. Coalescence of the outer wall was not observed among Type 2. Inner vesicles either display dark granular or smooth, hyaline wall(s). Inner vesicles uncommonly display a second wall (Figure 4a). In particular, this specimen displays vesicles that are encapsulated in coalesced second walls. The specimen in Figure 4b displays three inner vesicles (yellow arrowheads) with dark, granular walls surrounded by a second thinner wall; the inner vesicles are positioned off-center in their respective outer walls. Small carbonaceous masses are also included in the main spheroid (Figure 4c), a situation similar to Type 1, and within inner vesicles (Figure 4a).

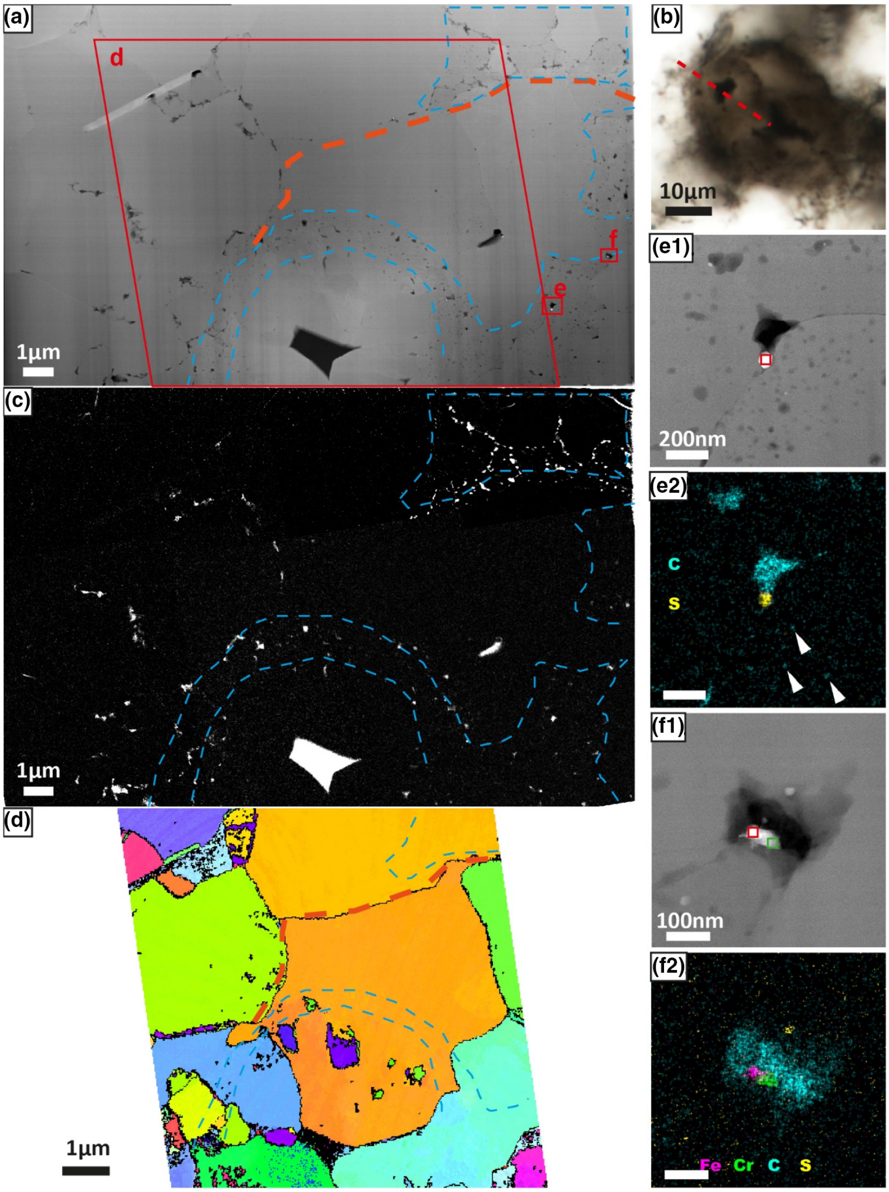

FIGURE 3 Analytical TEM of a Type-1 spheroid. Sample WF4-4. (a) HAADF STEM image of the FIB section indicated with red-dotted line in b. Inner spheroid boundaries show dark (carbonaceous) granules in quartz (grey). In light-grey, a (phyllo?)silicate. (b) Photomicrograph of the specimen indicating the FIB section location. (c) Energy-filtered image of carbon in the FIB section (contrast and brightness modified on each image forming this mosaic, see also Figure S7d). (d) Nanodiffraction map (area boxed in a) showing crystal orientations with respect to *Z* axis, overlain with "grain-boundary" (black) map. The assignment of single crystals to single-colored areas in this figure is supported by the comparison of the diffraction maps along 3 axes and the unique diffraction patterns recorded in each area (Figure S7). In a and d, orange-dashed lines indicate carbonaceous matter distribution (evidenced at the same position in c) occurring mostly at grains boundaries in the outer wall. Blue-dashed lines indicate nanoparticulate distribution that shaped the boundary of an inner sphere, which is cross-cutting multiple quartz crystals. (e$_1$) Zoom on the carbonaceous particle in boxed zone in a. (e$_2$) STEM-EDX of (e$_1$), white arrowheads indicate smaller carbonaceous particles within quartz crystals. A nanosulfide is located at the grain boundary with carbonaceous matter. (f$_1$) Second boxed zone in a. (f$_2$) STEM-EDX map showing the position of sulfide (of Fe + Ni) as well as Fe + Sb oxide and Cr(+Ti, Fe, Zn) oxide; EDX spectra of these nanoparticles shown in Figure S8

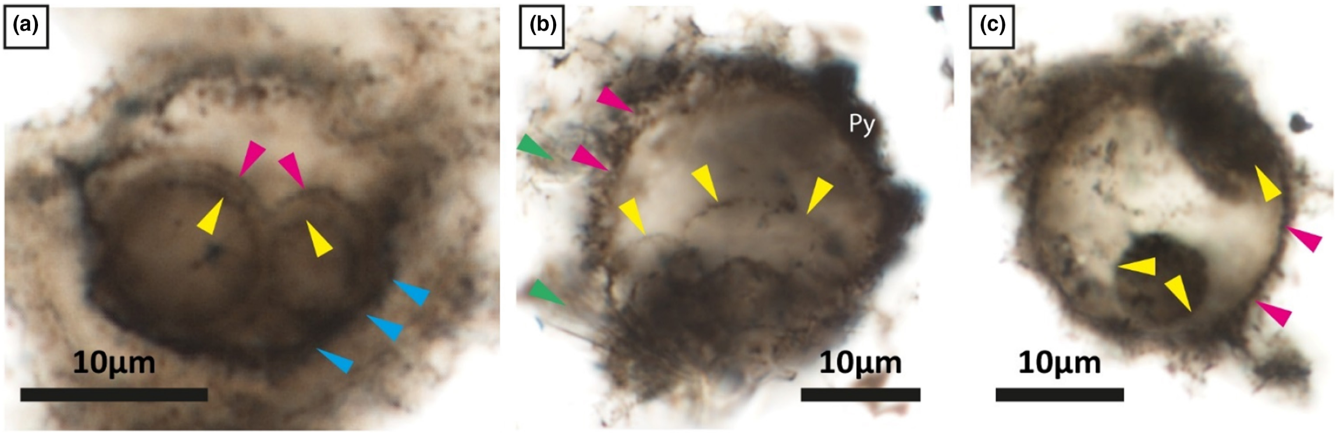

FIGURE 4 Type 2 spheroids. Photomicrographs. (a) Type 2 sphere that displays a dark wall with a smooth (blue arrowheads) to granular texture that encapsulates multiple (hemi)spheric vesicles with hyaline walls (yellow arrows). The two inner vesicles are encapsulated in a second wall that coalesces (pink arrowheads). Sample WF4-1. (b) Type 2 sphere that displays irregular outer wall (pink arrows), with variously sized internal vesicles and punctuated with probable phyllosilicate (green arrows) and pyrite (Py). Sample WF4-1. (c) Type 2 spheroid with smooth carbonaceous wall (pink arrowheads) and inner spherical carbonaceous vesicles (yellow arrowheads). Sample WF4-4

Our most striking Type 2 (Figures 4a, 5) specimen reveals through FIB sectioning a zone of well-defined, almost continuous outer carbonaceous wall where carbonaceous matter is constrained between micrometric to sub-micrometric quartz crystals (outlined in blue in Figure 5a). This outer wall may be less continuous in other parts of the sphere, as suggested by the granular aspect under the optical microscope (Figure 4a). In addition, equant quartz faces appear locally corrugated in contact with this outer carbonaceous wall, which also traps quartz nanocrystals. A fringe of coarse quartz crystals, sometimes forming crescent-shaped boundaries lies outside the carbonaceous wall with little carbonaceous matter at their grain boundaries other than those contiguous to the wall (outlined in blue in Figure 5a and f). In contrast, smaller, sub-rounded crystals lie on the inner side of the wall (Figure 5f). Two inner vesicles have inner walls (outlined in yellow in Figure 5a) of nanoparticulate carbonaceous matter that passes through multiple micrometric quartz grains in which they are partly embedded (Figure 5a, f), similar to the walls in Type 1. The two inner vesicles are embedded in a shared (coalescent) second wall (outlined in pink in Figure 5a) that also displays a hemispherical protuberance (at the top) that we have confirmed with multiplane optical imaging (not shown). This second inner wall displays a texture that alternates between bands of nanoparticles included in quartz and discontinuous nanofilms of grain-boundary carbonaceous matter (Figures 5a, d, e, f). It should be noted that in spite of its more particulate nature, the inner vesicle walls appear smoother at the micrometer scale (Figure 5b) than the thicker, more continuous outer wall (Figures 5d). This is likely the result of a more localized preservation of the position of the inner-wall carbonaceous matter allowed by embedding in quartz crystals, whereas the distribution of the thick outer wall was likely disrupted by small displacement at the grain boundaries of quartz. This is evidenced by the spear-shaped part of an internal quartz crystal that pierces through the carbonaceous wall with local disruption of the wall continuity (red arrow in Figures 5d-f).

A second Type 2 specimen displays relatively similar characteristics (Figure 6). Its outer wall (pink outlines) is also mostly composed of grain-boundary carbonaceous matter (Figures 6c-f), whereas the inner wall (yellow outlines) sometimes passes through quartz crystals as bands of carbonaceous nano-inclusions (Figures 6c-f). A single coarse crescent-shaped quartz crystal fills the space between the inner and outer wall boundaries for a large fraction of the sphere perimeter (Fig. $6f_1$). Corroded quartz boundaries are visible along the carbonaceous patterns (Figures 6g, j). Nano-sulfides are also observed in association with carbonaceous matter in Type 2 spheroids (Figures 6k, l).

A third Type 2 specimen displayed a different wall structure where the walls of inner spheroids are sub-continuous similar to the outer wall (Figure 7). Nanoparticulate carbonaceous inclusions appear absent, but a mixture of nano-quartz and carbonaceous matter is included and/or embayed within a coarser quartz crystal (arrowed in Figure 7b, e). The outer wall of this specimen includes abundant Fe/Mg aluminosilicates (likely chlorites, Figure S12). A pyrite microsphere forms a bulge in the outer wall without disrupting the continuity of the latter (Figure 7c-d). The pyrite includes a spherical carbonaceous particle (Figure 7d, Figure S14) as well as nickel-arsenic sulfide and aluminosilicate nanocrystals (white arrowheads in Figure 7c, d, Figure S14).

### 4.2.3 | Type 3 spheroids

Type 3 comprises spheroids with two to three wall layers (Figure 8a, Figures S15–S16). These spheroids appear singly (Figure S16d) and as coalescent clusters of hemispheres (Figure 8a, Figures S15 and S16a-c). Coalescing patterns are recognizable in which two or

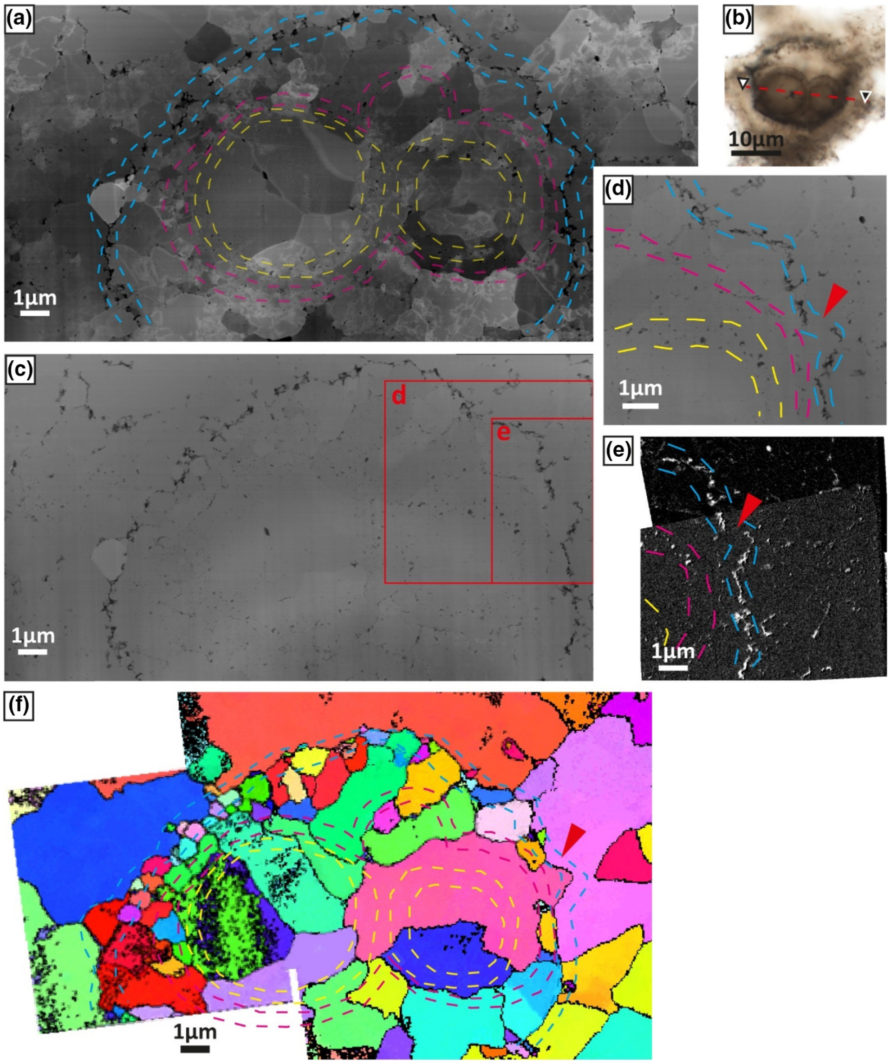

FIGURE 5 Type 2 spheroids in TEM. Sample WF4-1. (a) Dark-field STEM image of the FIB section prepared along the dashed line in (b). (b) Photomicrograph. (c) HAADF STEM image of (a). (d) Magnification of the left-boxed zone in (c). (e) Energy-filtered map of carbon in the boxed zone in c, red arrow indicates a possible tearing of the outer wall, this image is a mosaic of two picture acquired with the same contrast brightness correction (see also Figure S11). (f) Nanodiffraction map (*Z* axis, colors linked with Euler angles) of the FIB section overlain with the "grain-boundary" map. The assignment of single crystals to single-colored areas in this figure is supported by the comparison of the diffraction maps along three axes and the unique diffraction patterns recorded in each area (Figure S9). Dashed lines indicate the same positions in all panels, with: in cyan the outer wall, in pink the outer boundary of internal coalescent spheres, in yellow the inner boundary of internal spheres. (f) Shows that relatively large crystals surround the spheroid, while inner crystals appear smaller. The outer wall (blue-dashed) lies at grain boundaries with smaller quartz crystals whereas internal spheroid walls (pink- and yellow-dashed) cross-cut multiple quartz crystals

more inner spheres merge with apparent formation of carbonaceous septa (green arrowheads in Figure 8a, b, and Figure S15). In other cases, spheres coalesce without formation of a septum (Figure 8a, Figure S16a). Small carbonaceous masses are often seen inside the spheroids and in the surrounding nanoparticulate network.

We mapped the quartz grains with EBSD in a highly coalescent cluster of Type 3 spheroids (Figure 8). Partly rounded polycrystalline grains, that is, clusters of quartz grains where grain boundaries locally align in an arcuate fashion, fill the observed spheroids. The multiple, concentric wall of the coalescent spheroids partly occurs at grain boundaries, for example, along arcuate alignments of grain boundaries (yellow arrowheads in Figure 8b). In places, walls pass sequentially through multiple coarser crystals (pink arrowheads in Figure 8b), most likely as planes of nano-inclusions as observed in previous spheroid types. Similarly to the wall of Type 1 spheroids (Figures 2 and 3), the most peripheral wall as well as the inner walls of this coalescent Type 3 cluster occur along grain boundaries and also as inclusions (Figure 8b). In the example of the spheroid dyad occurring in the lower-left part of Figure 8a (Figure 8c-d), it is the darker (thicker?) inner wall that appears to occur along grain boundaries (Figure 8c-d, blue arrowheads), implying that the coalescent outer walls likely pass through the coarser surrounding crystals.

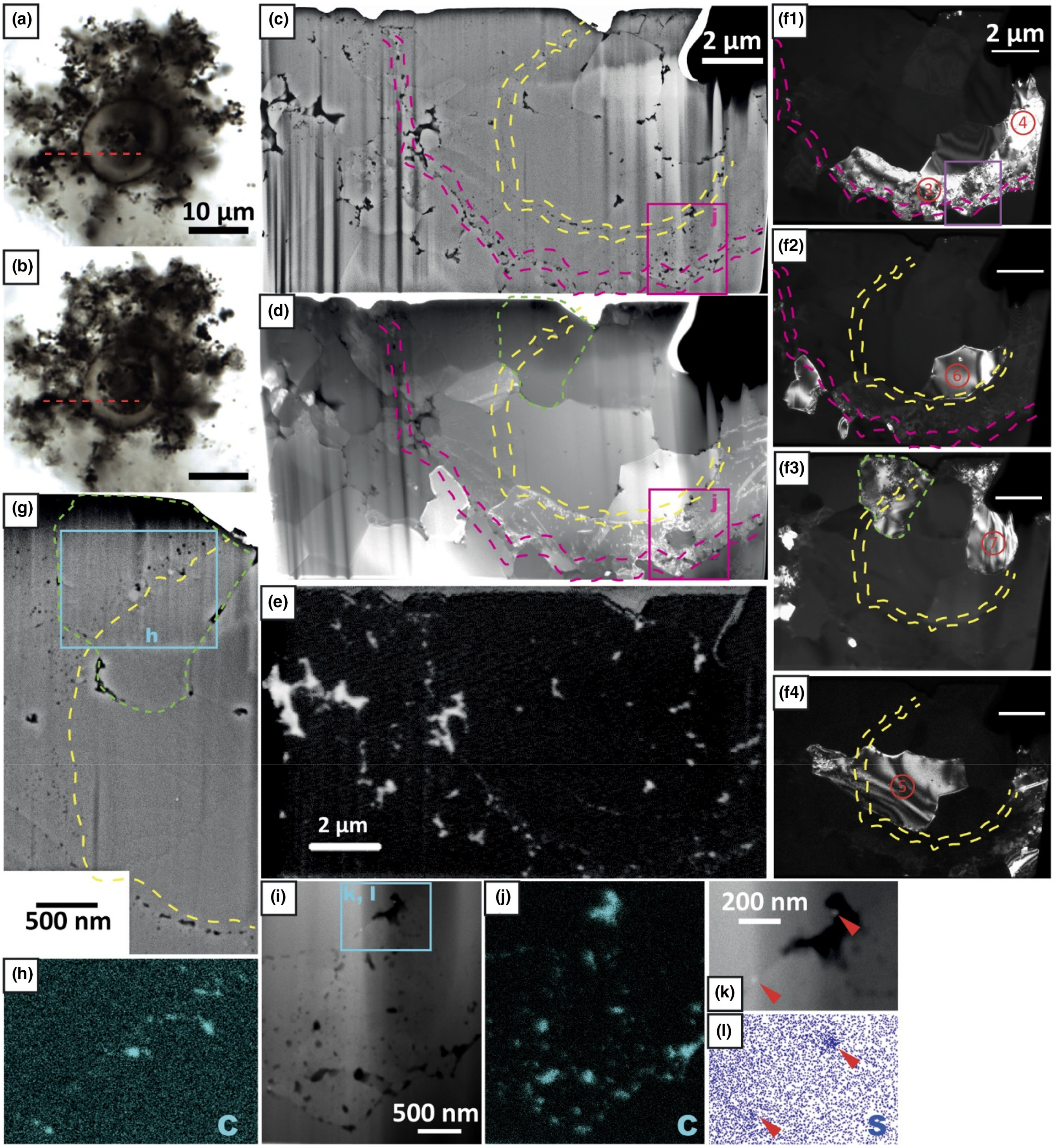

FIGURE 6 Type 2 spheres in TEM. Sample WF4-4. (a–b) Single-plane photomicrographs recorded at focal planes ca. 1.5 and ca. 4.5 µm below the thin section surface. (c–e) Images of the focus ion beam section cut along the red line in a-b: (c) HAADF STEM image, (d) dark-field STEM image, and (e) STXM map of aromatic carbon. Dashed yellow and pink lines outline carbonaceous particles or pores forming the boundaries of the inner and outer spheres seen in (a) and (b), respectively. ($f_{1-4}$) dark-field TEM images recorded by shifting the selected area aperture on the diffracted beam closest to the undiffracted beam using the diffraction patterns recorded in the circled areas as shown in Figure S10. (g) Left part of the inner boundary, HAADF STEM image. The quartz crystal outlined in green dashed line is the same as in ($f_3$). (h) Map of carbon recorded using STEM-EDX in the box in g. (i–j) HAADF STEM and corresponding STEM-EDX map of carbon in the pink-boxed zone (in c, d and $f_1$) showing carbonaceous particles embedded in a single quartz crystal. (k–l) Zoom on the boxed zone in J and associated map of sulfur showing nano-pyrites (red arrows)

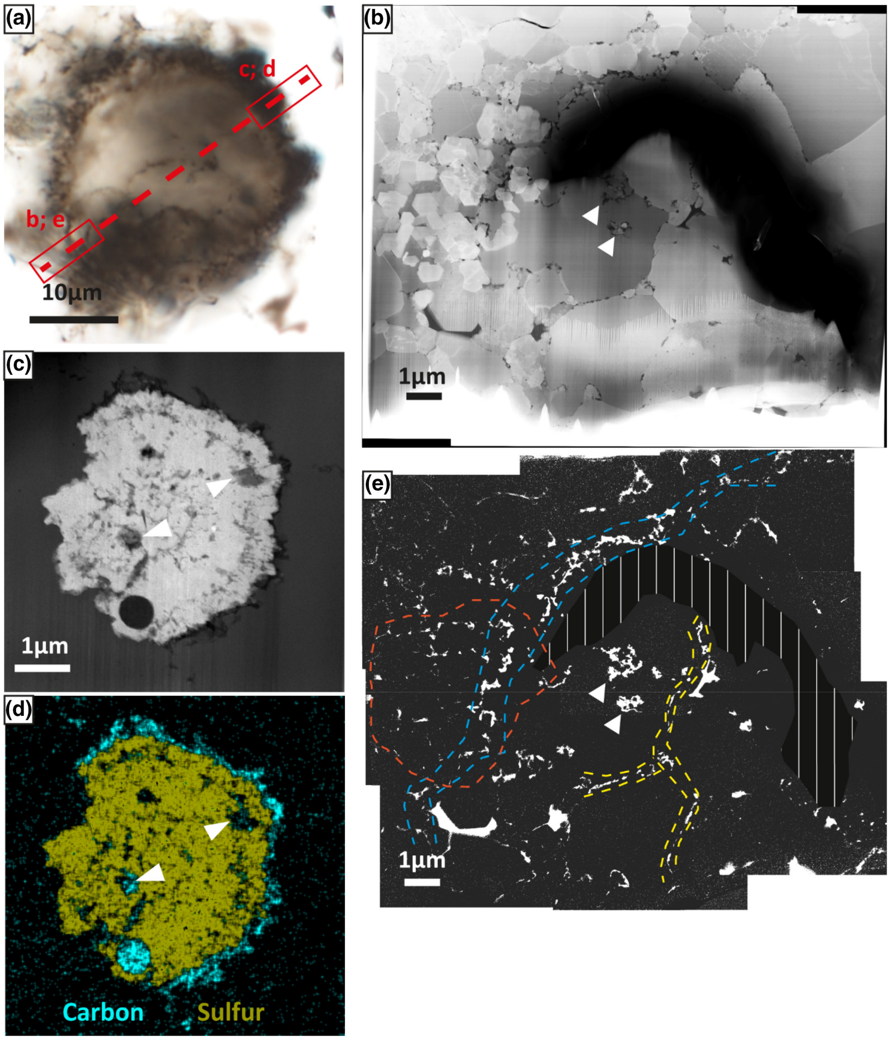

**FIGURE 7** Type-2 spheroid. Samples WF4-1. (a) Photomicrograph. (b) Dark-field STEM image of the focus ion beam (FIB) section prepared along the line in a (left box). Carbonaceous matter appears in black, sub-hexagonal chlorites (Figure S12) as lightest-grey, and quartz in shades of grey. (c) HAADF STEM image of the FIB section prepared along the line in a (right box), showing pyrite (light grey) within the carbonaceous wall (black) of the sphere. (d) STEM-EDX elemental mappings of wall-included pyrite sphere, white arrowheads indicate inclusions inside the pyrite. (e) Mosaic assembled from 9 individual EFTEM images of carbon, corresponding to the area shown in b. Each image was initially processed with a similar gamma correction, then they were assembled manually before individual change of contrast/brightness to each of the 9 images, and final homogenous gamma correction (see also Figure S13). Arrows in b, e show carbonaceous matter included and/or embayed within quartz

### 4.2.4 | Type 4 vesicles

Structures of Type 4 are spherical to sub-spherical vesicles that occur in a cluster shown in Figure 9a-c. Vesicles display a single- or a bi-layered granular wall (Figure 9b-c). Some vesicles share their outer wall and are only distinguished by their inner wall, which does not coalesce with adjacent vesicles (Figure 9b). A crown or a crescent of translucent (carbon-poor) quartz (<3 µm) usually forms between the inner and outer walls. Such clusters spread vesicles in three dimensions, which are visible through deepening focus and best seen with CLSM (Figure 9). The distinguishing feature of this type is the presence of discontinuities and wrinkles in the innermost wall (Figure 9c). Discontinuities in the inner wall sometimes form multi-micrometric openings (see opposite of the pink arrows in Figure 9b). Micrometric carbonaceous masses also occur in these structures and in the surrounding nanoparticulate network (Figure 9c).

An FIB section cut at the interface between several vesicles of the cluster in Figure 10 shows that both inner and outer walls are bound by sub-continuous films of carbonaceous matter occurring at the boundaries of quartz crystals (Figure 10). A thick carbonaceous mass is located at the bottom of the section that forms denticles surrounded by small subhedral quartz crystals. The presence of reticulated grain-boundary carbonaceous matter between the spheres makes it impossible in this FIB section to distinguish individual, coalescent or amalgamated outer walls. Finally, a coarse quartz grain fills most of the empty space within the vesicles numbered 1 and 4 (Figure 10b-c).

### 4.2.5 | Type 5 empty pustular spheres

Type 5 comprises a single, empty sub-spherical vesicle, ca. 110 µm in diameter at the observed cross-section (Figures 11 and 12). Its main, thicker wall displays depressions (green arrowheads in Figure 12) and pustules (yellow arrowheads in Figures 11 and 12). It is embedded in a network of nano-particulate to coarse carbonaceous matter, which includes smaller spheroids, possibly of Types-1 or 2 (Figure 11b). This nano-particulate organic matter appears to organize concentrically around a side of this vesicle, yielding a multi-walled aspect (Figure 11c). This multi-layered aspect is, however, seen only in surface view (Figure 11c) but not

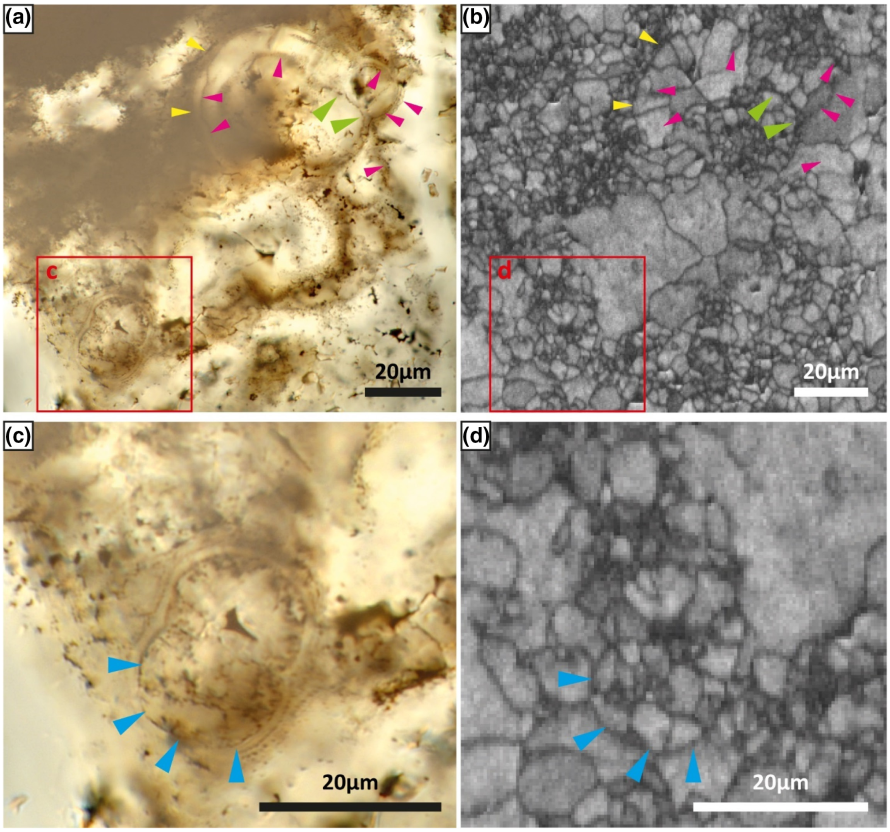

**FIGURE 8** Type-3 spheroid, sample WF4-3. (a) High dynamic range photomicrograph combination recorded at the surface of the section. (b) Electron backscattered diffraction (EBSD) band contrast image of the same zone. (c–d) Zoomed zone indicated by red boxes in a and b, respectively. Yellow and blue arrowheads highlight positions where carbonaceous walls occur at the grain boundaries of hemispherical polycrystalline quartz (see main text). Green arrowheads indicate a carbonaceous septum that lie at grains boundaries between two coalescent spheres. Pink arrowheads highlight positions where carbonaceous walls are partly included in single quartz crystals (these have been demonstrated as single crystals by homogenous color in EBSD IPF index images along three axes: Figure S15)

deeper in the thin section (Figure 12), and may be generated by a contrast artefact arising from the automated Z-brightness (gain) adjustment that is necessary to image deeper focal planes. Thus, the general aspect of the outer wall is single- and thick-walled (Figure 12).

Virtual slicing and 3D rendering of the CLSM image stack reveals that pustules in the main wall are vesicular (yellow arrowheads in Figure 12), that is, that they display an inner wall separated from the main (external) wall. Note the thickness difference between the inner wall of this pustule and that of the main wall (Figure 11c). In contrast, in the adjacent pustule (highlighted by green double-sided arrow in Figure 11a and c), the inner wall appears thicker than the outer wall.

In Figure 11, it appears that the wall is locally pierced, but this is likely an artefact generated by the reflection/absorption of the laser by opaque particles (including gold contaminants, Figure 11) at/near the surface, as shown by Figures 11d-e. A hemispherical depression in the main wall is also seen with virtual slicing and 3D rendering (green arrowheads in Figure 12e). The multiplane image stacks recorded with transmitted white light and CLSM are shown as Video S1 and Video S2, respectively.

Imaging of quartz crystal domains with EBSD, coupled to CLSM showing carbonaceous matter (Figure 11c, d, Figure S17) revealed that the quartz crystal size is similar within the vesicle and in the clear-quartz surrounding matrix. In contrast, smaller quartz occurs in the nanoparticulate carbonaceous network surrounding the vesicle. Moreover, a coarser quartz crystal occurs in the pustule outlined by yellow arrowheads in Figure 11d where it embeds part of the inner wall (likely as a plane of nano-inclusions) and embays another part of this wall. The main carbonaceous wall of the large spheroid lies integrally at grain boundaries (blue arrowheads in Figure 11d, two tentative positions in the lower-left corner due to possible multilayered artefact). Finally, an arcuate series of grain boundaries inside the vesicle (pink arrowheads in Figure 11c, d) appears devoid of carbonaceous matter, unlike those observed in previous spheroid types.

## 5 | DISCUSSION

The cellular nature of Paleoarchean microspheres has been debated, competing with the alternative hypotheses of carbonaceous coating of abiotic silica spherulites (Brasier et al., 2005; Buick, 1990) and carbonaceous coating of vesicles in volcanic ashes (Hickman-Lewis et al., 2016; Wacey et al., 2018a, b). Here, we found no evidence of a (volcano)clastic component in the black chert layer hosting the spherical microstructures. A region of botryoidal quartz coated with carbonaceous matter is present at the edge of the WF4 sample (Figure S1). Silica botryoids in another SPF chert displayed hemispherical, coalescent quartz microstructures coated by carbonaceous matter (Sugitani, Mimura, Nagaoka, Lepot, & Takeuchi, 2013). Together with the presence of carbonaceous veins argue that carbonaceous matter migration is a plausible route for the formation of various carbonaceous pseudofossils in the studied rock. Based on the textural features observed and summarized in Table 1, we discuss the

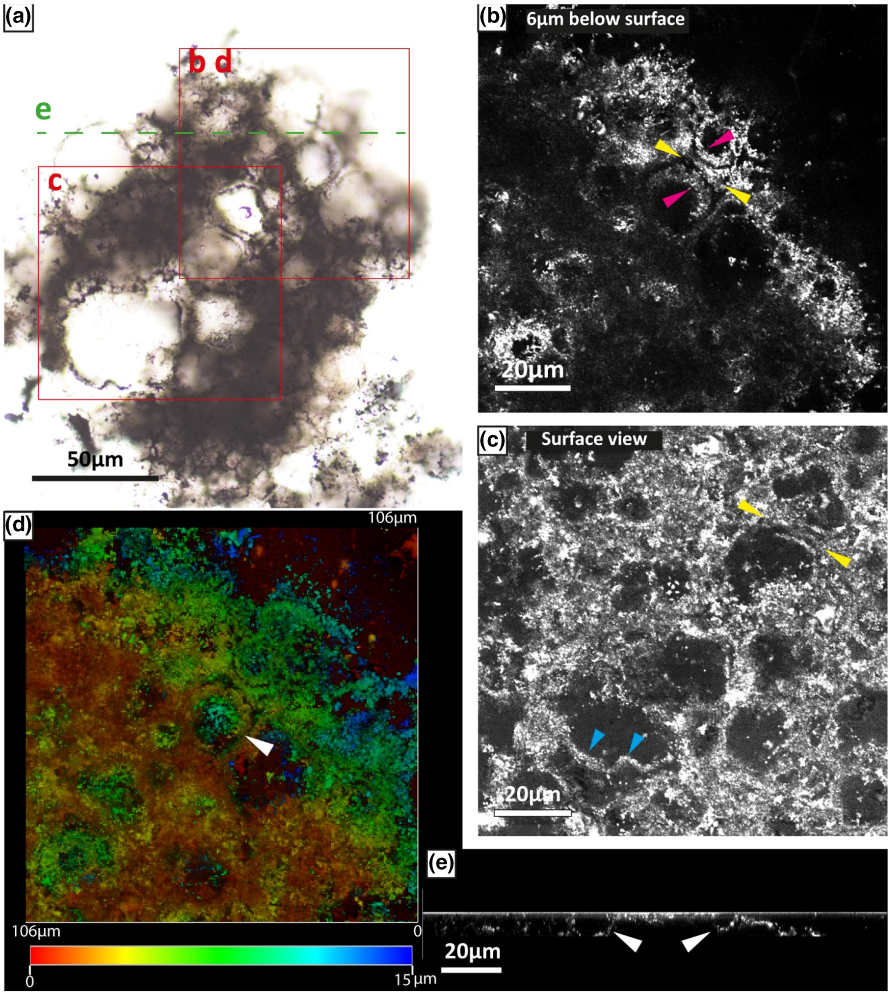

FIGURE 9 Cluster of Type 4 spheroids. Sample WF4-1. (a) Photomicrograph. (b) Confocal laser scanning microscopy (CLSM) image of the boxed area in a, pink arrowheads indicate inner carbonaceous walls that are surrounded by a carbonaceous-matter-free quartz ring, and an outer wall (yellow arrowheads) that appears coalescent with that of adjacent spheres. (c) CLSM image, blue arrowheads indicate the wrinkled part of a sphere. Yellow arrowhead indicates the coalescence of the outer wall of two adjacent spheres that appear wrinkled and deformed. (d) 3D reconstruction of CLSM stack. Rainbow scale indicates the depth of the signal-generating carbonaceous structure, with red from the surface of the thin section and blue from the deeper part of the image stack, white arrowhead exemplifies a well-rounded sphere within the cluster. (e) Virtual section of the confocal image stack obtained at the vertical of the lines on the left; white arrowheads point out sphere boundaries

following hypotheses for the morphogenesis of Type 1–5 spheroids: (i) organic matter migration associated with a mineral template or matrix, (ii) cellular origin, and (iii) self-assembly of organic biomorphs.

Criteria to distinguish microfossils from abiotic biomorphs have most recently been reviewed in Rouillard et al. (2021). Geological context criteria for microfossils are fulfilled for the observed structures, including embedding in a sedimentary rock, minimal size, carbonaceous composition, hollow structure and population-forming distribution (for Type-1-3, with multiple specimens in specific laminae). None of these contextual criteria rule out abiotic morphogenesis. Additional morphological criteria and inferences on formation and/or preservation will be sought here by discussion of the carbonaceous textures in the context of their host quartz structures.

## 5.1 | Origin of pyritic spherulites

The fibrous, multilayered pyritic spherulites belong to colloform structures, which are abundant in hydrothermal deposits but also found in modern/ancient sediments (Gao, Huang, Wang, & Gao, 2016). Although the exact mechanisms allowing the growth of such structures has not been resolved, plausible hypotheses include biogenic, organic-templated, and abiogenic routes (Gao et al., 2016). Pyrite framboids with layered and fibrous overgrowths, named sunflower pyrites, may also form in sedimentary environments (Merinero, Cárdenes, Lunar, Boone, & Cnudde, 2017). However, the observed spherulites are distinct from sunflower pyrites in that they commonly display a non-pyritic core and they do not show clearly central framboids. Moreover, pyrite spherulites embedded Ni-As-sulfides as well as various Cu(Fe)-sulfides, and the pyrite sphere embedded in a Type-2 spheroid (Figure 7) includes (Fe?)-Ni-As-sulfide. This assemblage is suggestive of hydrothermal input (Beveridge, Meloche, Fyfe, & Murray, 1983; Fontboté, Kouzmanov, Chiaradia, & Pokrovski, 2017). A reticulate network of carbonaceous matter linking and partly coating pyritic spherulites with dense carbonaceous masses (Figure 1) and carbonaceous droplets or particles occurring within single spherules (Figure 1 and Figure S2a-c) suggests that these pyrite spherulites are associated with migrated organic matter. The latter may have participated in the sulfide morphogenesis. In addition, coalescence structures are observed in spherulitic pyrites (Figure 1) that strongly evoke the patterns observed in Types-1-3 carbonaceous spheres. However, the carbonaceous coating of pyrites appears only partial, and their diameter is always smaller (<10 μm) than the

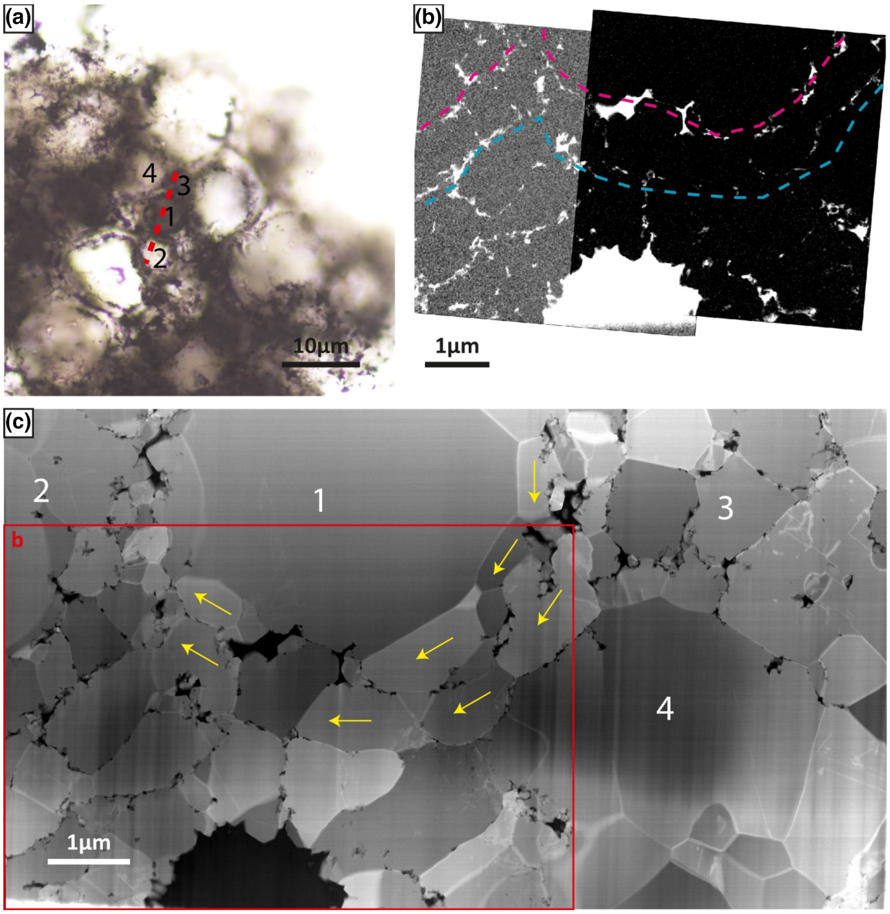

**FIGURE 10** Type 4 spheroids in TEM. Sample WF4-1. (a) Photomicrograph: Central part of Figure 9a, red dashed line indicates the section. Numbers indicate the positions of each sphere cut across by the FIB section. (b) Energy-filtered carbon map (red boxed zone of c). Pink-dotted lines outline the inner walls, blue-dotted line outline the outer wall. (c) Dark-field STEM image. Numbers indicate parts of the spheres annotated in a that are intercepted by the FIB section. Arrows indicate platy quartz crystals on each side of the wall of spheroid number 1

carbonaceous Types-1-5 spheres (>15 µm). Pseudomorphosis of such carbonaceous spherulitic pyrites by quartz thus cannot readily explain Types-1–5 microstructures.

## 5.2 | Carbonaceous masses and migration

### 5.2.1 | Origin of carbonaceous masses?

Type 1 spheres with large internal carbonaceous masses can be related to spheroidal microstructures from the Onverwacht Group of South Africa (e.g., Figure 2b in Engel et al., 1968) interpreted as dubiofossils (Nagy & Nagy, 1969). The carbonaceous masses within the Types 1–3 spheroids, closely associated with Type 4 spheroids (Table 1), and in the Onverwarcht specimens may have formed through post mortem condensation and/or aggregation: dense carbonaceous masses have indeed been observed during experimental fossilization of cyanobacteria (Oehler, 1976). They may also form by bitumen addition in porous microfossil molds (Rasmussen et al., 2021). Here, we have not observed nanopores in these carbonaceous masses that may argue for a pyrobitumen origin (Bernard & Horsfield, 2014). However, we cannot rule out pyrobitumen because (1) our FIB section thicknesses and analytical conditions may not have allowed observation of the smallest nanopores (Figure 3d in Bernard and Horsfield (2014)) and (2) nanopores may have become occluded by regional metamorphism and/or displacement by quartz growth.

### 5.2.2 | Migration from central masses?

Carbonaceous halos observed around stellate carbonaceous masses in Paleoarchean chert have been interpreted to result from displacement of carbonaceous matter away from a central core of organic matter during the growth of spherulites of chalcedony (Buick, 1990), based on the experiments of Oehler (1976). Dense carbonaceous masses found at the center of single and coalescing siliceous hemispheres outlined by carbonaceous matter, observed in Paleoproterozoic cherts by Tyler and Barghoorn (1954) have been re-interpreted as pseudofossils of botryoidal chalcedony by Mendelson and Schopf (1992). Similarly, migration of soluble organic matter at the grain boundaries of quartz surrounding filamentous Paleoproterozoic microfossils has been proposed to explain tubular halos surrounding the fossils (Knoll, Strother, & Rossi, 1988). However, in a similar microfossil assemblage, no difference in nanoquartz texture was observed between the internal tubes, external halos and microfossil periphery (Fadel, Lepot, Busigny, Addad, & Troadec, 2017). This has been used to argue that migration at grain boundaries could not explain the halos, which could represent primary sheath anatomy (Fadel et al., 2017). In this case, the migration model would require that different precursor silica textures (e.g., with variable porosity locally allowing for sequestration of halos) would have led to the same nanocrystalline quartz.

Alternatively, the extent of the halos may have been controlled by diffusion of carbonaceous matter in silica gel rather than the

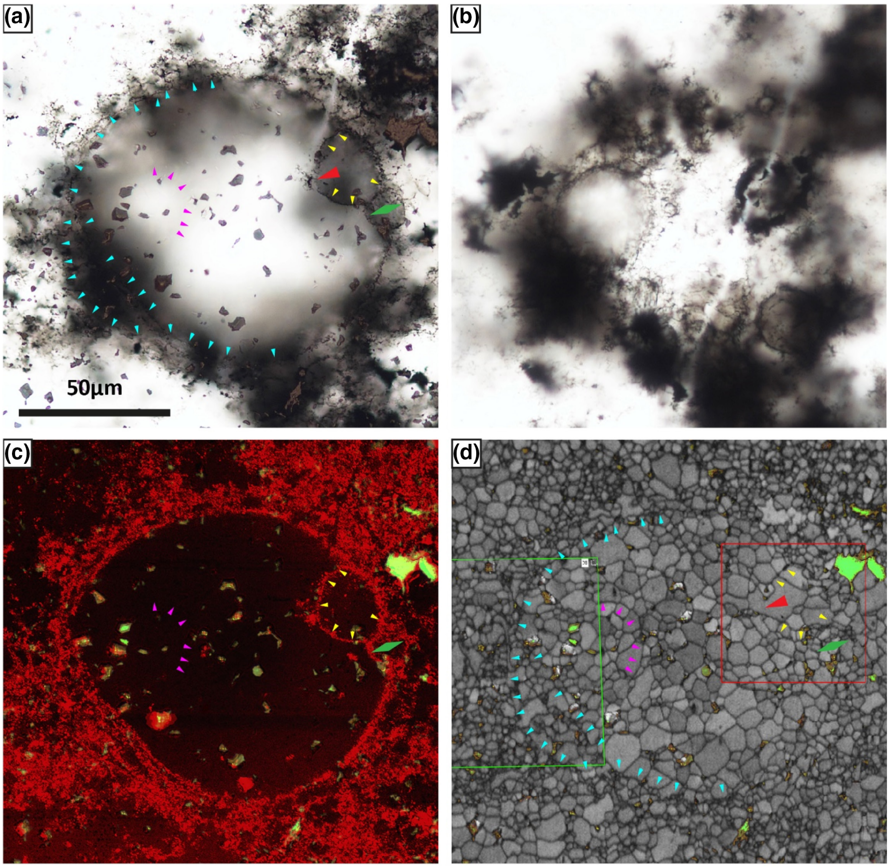

FIGURE 11 Type 5 spheroid. Sample WF4-1. (a–b) Photomicrographs taken at different focal planes: (a) surface of the thin section, (b) 33 µm below the surface, showing smaller spheroids below the larger Type 5 spheroid. (c) Confocal laser scanning microscopy (CLSM) image of the same zone at the surface of the thin section. (d) Electron backscattered diffraction (EBSD) band contrast image of the same zone revealing quartz grain boundaries. This image comprises the overlay of two EBSD mappings, one recorded first in the zone of the green box, and the larger field recorded subsequently (due to deposition of carbon during acquisition of the first image, the contrast was degraded in the green-boxed zone of the larger field). In c–d, the reflected-light photomicrograph is overlain, showing residual goal coating in yellow-green. In a through d, yellow arrowheads indicate an inner spherical pustule; the red arrows indicate a position where the wall of this pustule is partly included in a single quartz crystal. The single crystal nature of this grain is demonstrated by its homogenous color in EBSD orientation maps along three axes (Figure S17). Pink arrowheads show an arcuate series of grain boundaries as seen in c–d that could correspond to the wall of a carbon-poor internal quartz spheroid. Blue arrowheads indicate the apparent multilayered aspect of the outer wall in the left part of the spheroid. The twin green arrowheads in a, c, d indicate another small pustule

textures of the growth front of silica. Such diffusion front(s) in silica gel have been suggested as possible drivers for the formation of ellipsoidal silica concretions with internal carbonaceous cores (Yoshida et al., 2021). They may also explain the carbonaceous banding observed in some Paleoproterozoic granules (Papineau, She, & Dodd, 2017), or the Liesegang rings of Fe-/Mn-oxides formed for example around tubular structures in some agate (Kile, 2002). Thus, diffusion of carbonaceous matter away from carbonaceous masses in silica gel prior to quartz crystallization could explain peripheral carbonaceous walls.

The marginal carbonaceous walls of Type 1 spheroids (Figures 2 and 3) could thus represent organic particles/droplets that (i) migrated radially through diffusion in silica gel (or in another poorly crystalline precursor to quartz), (ii) migrated along with the growth front of siliceous spheroids, or (iii) accreted on silica growth fronts. In the first two hypotheses, the central masses represent the most plausible carbon source, although accretion could also proceed from ambient fluids. Type 3 spheroids and the internal vesicles of Type 2 spheroids are multilayered (Figures 4a, 5–8), a feature that can also be generated with diffusion fronts (Papineau et al., 2017). In addition to botryoidal calcedony (Kile, 2002), growth of amorphous opal may serve as a template for spherulitic growth of silica (Jones & Renaut, 2007) whereby the internal growth banding may sequester ambient carbonaceous matter to form multiple carbonaceous walls.

## 5.3 | Coalescence patterns

### 5.3.1 | Coalescence in Type 1 and 3 spheroids

Types 1 and 3 specimens are similar in that they comprise multiple examples where their carbonaceous wall(s) display coalescence

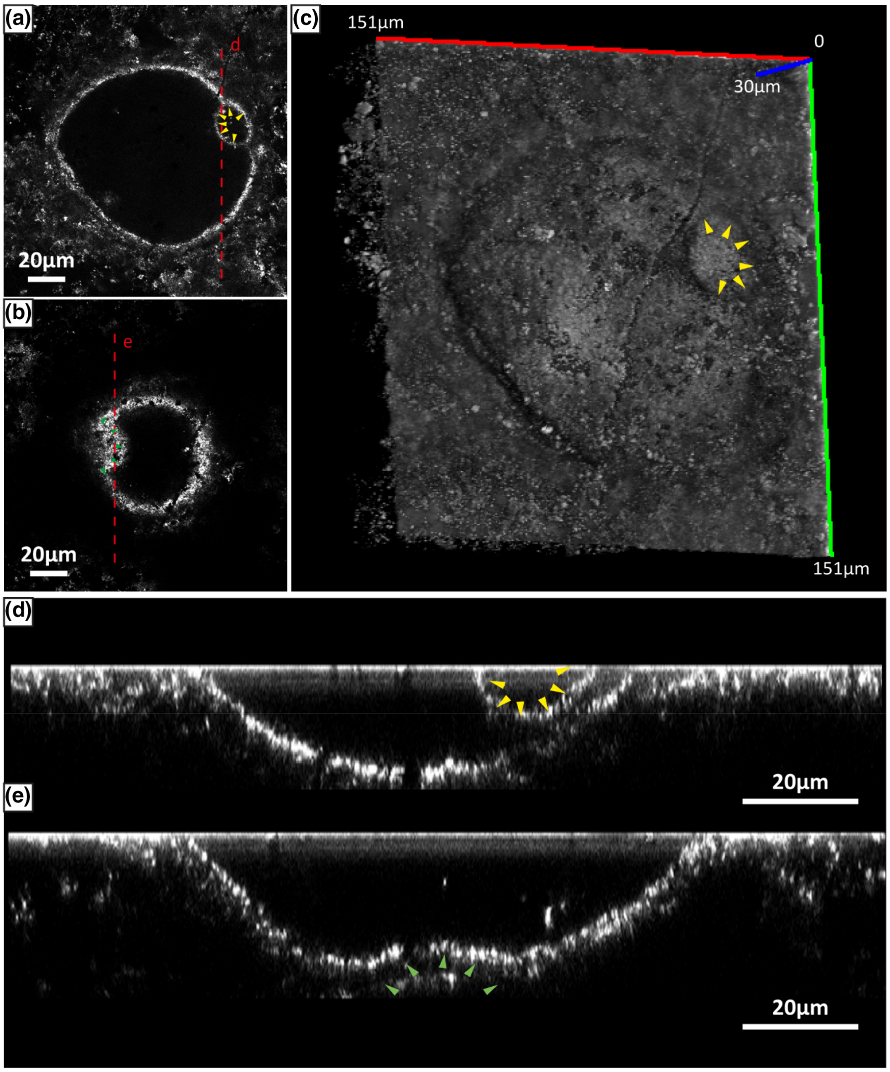

**FIGURE 12** Detailed confocal laser scanning microscopy imaging of the Type-5 spheroid, as shown in Figure 11. (a–b) Single confocal images (a) 4.5 µm below the surface, (b) 21.80 µm below the surface. (c) 3D reconstruction of the structure seen from the bottom. (d–e) Virtual slices extracted along the lines in a–b. Yellow arrowheads in d indicate a pustule in the main wall, green arrowheads in e indicate a depression in this wall

patterns (Figures 2, 8). Such coalescence of spheroids is well known in abiotic opal (c.f. Figure 7E in Jones & Renaut, 2007 versus Figure 2b herein), and carbonaceous coating of such spheroids may explain coalescence of single as well as multiple carbonaceous walls. Diffusion of organic matter in silica gel can also explain coalescence patterns, as observed in Liesegang ring structures (Kile, 2002; Papineau et al., 2017). Coalescence patterns are also observed in siliceous botryoids of the 1.88 Ga Gunflint Formation displaying single (Mendelson & Schopf, 1992 versus Tyler & Barghoorn, 1954) or multilayered (Javaux & Lepot, 2018; Rasmussen et al., 2021) walls. As discussed above, the presence of a plausible carbonaceous source in central masses is by itself proof that migration generated the outer walls of the carbonaceous spheroids, as the former can be explained by taphonomic processes in microfossils. However, the observed wall coalescence patterns indicate abiotic morphogenesis in Type 1 and 3 spheroids, as well as in the internal vesicles of Type 2 spheroids. Quartz botryoids coated by single, thick (Sugitani et al., 2013) or nanoparticulate (Wacey et al., 2012), carbonaceous layers in the SPF and other Paleoarchean cherts (Buick, 1990) most plausibly formed carbonaceous walls through migration.

Some Type 3 spheres display dyad shapes with thin carbonaceous septa (Figure 8c-d; Figure S16b) that strongly evoke microfossils. These Type-3 dyads are remarkably similar to some coccoid-like microstructures in 3.0 Ga cherts (Ueno, Isozaki, & McNamara, 2006). However, the singleton Types 1 and 3 spheroids and Type 3 dyad structures are associated, often closely, with coalescence of multiple (>2) Type 1 and 3 spheroids of widely distinct sizes (Figure 8, Figure S4). The latter forms clusters where the outer shape is not sub-spherical. This, together with the finding of nonspherical Type 1-like structures (Figure 2b, left, Figure S4), strongly argues against cellular division or taphonomic processes as the origin of coalescence patterns in Type 1 and Type 3 spheroids.

### 5.3.2 | Internal vesicles in Type 2 spheroids

The internal aspect of our Type 2 microspheres is different from that of spheroids described previously in the 3.0 Ga Farrel Quartzite and the SPF (Lepot et al., 2013; Sugitani et al., 2007, 2010; Wacey et al., 2018a) in that they display internal vesicles. Non-coalescent internal vesicles (Figure 4b) are strongly reminiscent of those

**TABLE 1** Summary of the main textural features of five carbonaceous spheroid types

| | Type 1 | Type 2 | Type 3 | Type 4 | Type 5 |
|---|---|---|---|---|---|
| **Distinctive features** | *Single-walled spheroids ± unusual forms* | 1–5 internal vesicles, coalescent | Multi-layered walls, *coalescent clustering* | **Wall folding**, clustering | Outer wall with pustules and depressions |
| **Carbonaceous masses** | Multi-micrometric | Sub-μm | Sub-μm to multi-micrometric | Sub-μm to multi-micrometric | No |
| **Sub-continuous wall at quartz boundaries** | | Partial outer wall, partial inner vesicle walls, local *pyrite bulge without tearing* | *No TEM* | Inner wall **folded**, possibly outer wall | For full cross section |
| **Arcuate alignment of quartz boundaries** | Yes | Crescent-shaped crystals along outer wall | Along inner/outer walls | Yes, of platy crystals between inner/outer walls | Along outer and pustule walls, within spheroid (non-carbonaceous) |
| **Nanoparticulate walls with embedding in quartz** | Outer wall | Parts of internal vesicles and outer wall | Inner and/or outer walls | | Only on thinner wall of pustule |
| **Coalescence** | *Wall* | *Only of internal vesicles* | *Inner and outer walls (multi-layered), with/without septa* | Only of outer wall/sheath | **No** |
| **Additional mineralogy** | (phyllo?)silicate, Fe–Ni–S, oxides of Fe + Sb and Cr(+Ti, Fe, Zn) | Zoned chlorites, sulfides (Fe, Fe–Ni, Fe?–Ni–As) | *No EDX data* | | *No EDX data* |

*Note:* Bold text indicates the criteria interpreted as most consistent with biogenicity and italic-underlined text indicates features interpreted as abiotic.

in the Paleoproterozoic microfossils *Leptoteichos golubicii* and *Huroniospora* (Knoll, Barghoorn, & Awramik, 1978). In these microfossils, internal carbonaceous granules, sometimes spherical, have been interpreted as collapsed intracellular material as occurs in taphonomic experiments (Knoll et al., 1978). However, in our material, the association of multiple internal vesicles that share a second wall (Figure 4a) and the existence of multiple internal vesicles with off-centered secondary walls (Figure 4b) cannot be explained by contraction of internal cell material (Knoll et al., 1978) and/or internal protoplast condensation (Pang et al., 2013). Moreover, Ueno et al. (2006) reported spheroids encapsulating inner hemispheres, similar to that of Figure 4a, in the 3.0 Ga Cleaverville Formation. However, the multiple internal vesicles sharing a second wall may form by overgrowth of coalescent opal spheres by cement (Figure 11 in Jones & Renaut, 2007) associated with coating of mineral interfaces by reticulated carbonaceous matter. In addition, structures of sphere dyads associated within a coalescing second wall similar to vesicles in Figure 4a, and vesicles that appear off-centered in a second wall similar to those of Figure 4b have been observed in experiments of abiotic co-polymerization of amino acids (Fox & Yuyama, 1963). Thus, abiotic structuration of organic vesicles may also have occurred prior to formation of the silica mineral (c.f. 5.8). Although internal vesicles could have been shaped by growth of silica and/or abiotic polymerization, this does not preclude that they may have grown within the wall of a decaying microfossil. Growth of silica spheres has been observed in/on filamentous cyanobacteria during experimental silicification with overall preservation of the filamentous morphology (Oehler, 1976).

### 5.3.3 | Coalescence in Type 4 spheroids

Type 4 spheroids only display coalescence of their outer walls, not of their inner walls (Figure 9). This strongly contrasts with the coalescence patterns of Types 1 and 3. It can be reconciled with biogenic morphogenesis, whereby the inner spheroids represent cells and the locally coalescent outer walls may represent fossils of polysaccharide sheath(s) (Stanier, Kunisawa, Mandel, & Cohen-Bazire, 1971). Nevertheless, this coalescence pattern cannot be ruled out as an abiotic feature, as suggested for those observed in Type 1 through Type 3 spheroids.

## 5.4 | Intracrystalline carbonaceous nanoparticles

The outer walls of Type 1 and Type 3 spheroids, most of the walls of internal vesicles of Type 2 spheroids, and parts of the outer walls of Type 2 spheroids are formed by carbonaceous nanoparticles (Table 1, Figures 2-8). Such a speckled appearance was observed in abiotic spheroids including discontinuous carbonaceous coatings onto spherical vesicles in tephra of the 3.47 Ga Dresser Formation (Wacey et al., 2018b) and on quartz botryoids of the

SPF (Wacey et al., 2012). These carbonaceous nanoparticles outlining spheroids/vesicles are commonly partly included in multi-micrometric quartz crystals (Figures 2c, d, 3d), the growth of which has thus not been limited by the presence of a denser carbonaceous wall. This cross-cutting relationship and the nanoparticulate carbonaceous texture appear particularly consistent with diffusion of minute amounts of carbonaceous matter in poorly crystalline silica (gel?) prior to quartz crystallization. Nevertheless, such a nanoparticulate aspect of organic matter has also been observed in fossil filamentous sheaths of Paleoproterozoic microfossils (Fadel et al., 2017; Lekele Baghekema et al., 2017) where it could arise from impregnation of dehydrating sheath polysaccharides with silica nanoparticles (Gong et al., 2020; Wacey et al., 2012). In contrast with the SPF intracrystalline particles, in these Paleoproterozoic fossil sheaths the carbonaceous nanoparticles occur at the grain boundaries of nanocrystalline quartz. Additional studies are needed to assess the possibility that nanoparticulate walls embedded in multi-micrometric quartz could occur in genuine microfossils.

### 5.5 | Sub-continuous carbonaceous walls at crystal boundaries

Previously described spheroids of SPF cherts commonly display a poor wall preservation with granular and discontinuous boundary (Sugitani et al., 2010), although large (>10 µm) spheroids with smooth walls have recently been extracted from SPF cherts (Delarue et al., 2020). Spheroids observed in siliceous cements of a SPF sandstone also display sub-continuous carbonaceous walls (Wacey et al., 2011, 2012). Almost continuous outer wall segments occur in Type-2 specimens (Figures 4-7, Figure S11), whereas other parts of the same walls appear nanoparticulate (Figure 5c, d) to granular (Figure 4a, upper half). Such disruption of organic walls has been reported in Neoproterozoic acritarchs (Grey & Willman, 2009), which can yield a granular aspect with local enrichments of organic matter. Sub-continuous walls are also seen with TEM and/or CLSM in complete cross-sections of Type 4 and Type 5 spheroids (Figures 9-12). Such sub-continuous walls are similar to those observed in well-preserved (Lepot et al., 2017; Wacey et al., 2012) or partially preserved (Lekele Baghekema et al., 2017) Paleoproterozoic microfossils, and coalescent spheroids of the SPF sandstones (Wacey et al., 2011, 2012). This characteristic was also noticed after acid extraction process in the SPF, where alveolar hemispheres have been interpreted to result of a partial conservation of the wall (Delarue et al., 2020). However, this heterogeneous distribution of carbonaceous matter may also arise from heterogeneous carbonaceous coating of a spherulitic mineral template.

Consistent with low-grade metamorphism at temperatures exceeding 300°C (Lepot et al., 2013), quartz crystals associated with the SPF microstructures are coarser (ca. 0.5 to >10 µm, mostly >1 µm) than those associated with Paleoproterozoic microfossils, which are mostly ~0.01 to a few µm in size (Fadel et al., 2017; Lekele Baghekema et al., 2017; Lepot et al., 2017; Wacey et al., 2012). The sub-continuous carbonaceous outer walls, when present in Type-2, 4 and 5 spheroids, lie at the boundaries of quartz crystals, often aligned in an arcuate fashion along the walls (Figures 5f, 6, 10c, d), and sometimes elongated along the walls (Figures 5f, 6f$_1$, 10c). Multi-micrometric quartz crystals have been observed in *Huroniospora* microfossils that are coarser than matrix quartz and that display an arcuate boundary with the continuous cell wall (Lekele Baghekema et al., 2017; Lepot et al., 2017). A similar quartz texture is observed in coalescent Type-3 spheroids, but in this case parts of the walls are locally cut across by quartz crystals (Figure 8b). Moreover, the micrometric quartz crystals that occur in contact with the sub-continuous wall appear corroded. A similar pattern was observed in quartz crystals in a lenticular microstructure of the same sample (Sugitani et al., 2015a). Such corroded carbonaceous patterns have been interpreted as the result of recrystallization into relatively coarse quartz, with embayment of organic matter adjacent to places where submicrometric, early diagenetic grains became parts of coarser quartz crystals. This model suggested by Wacey et al. (2012) is supported by the observation of various quartz growth “stages” associated with Paleoproterozoic microfossils (Lekele Baghekema et al., 2017).

Interestingly, a pyrite microsphere is wrapped by the outer, sub-continuous wall of a Type 2 spheroid (Figure 7, Figure S14). The latter remains continuous around the pyrite. Should the organic wall have been present before the growth of pyrite, we may expect it would have been torn by the local increase in surface caused by pyrite growth, in a fashion similar to the tearing by quartz growth observed in Figure 4 (arrowed). This continuity of the carbonaceous wall at the surface area of the pyritic bulge thus suggests that the carbonaceous matter was deposited during or after the growth of pyrite. The spherical carbonaceous inclusion in this pyrite microsphere further suggests the co-deposition of pyrite and carbonaceous matter. Furthermore, sub-continuous carbonaceous walls occur on inner vesicles along crystal boundaries in some Type 2 spheroids (Figure 7). As discussed above, the multiplicity and coalescence patterns of these vesicles argue for an abiotic shaping. Thus, sub-continuous carbonaceous walls may not suffice as a cellular identification criterion, in particular for specimens with coalescence patterns.

### 5.6 | Case of Type 4 spheroids

In Type 4 specimens, a quartz ring bounded by two sub-continuous (Figures 9, 10) carbonaceous boundaries comprises subhedral quartz crystals smaller than ca. 1 µm, whereas the inner part of the structure displays coarser crystals (up to ca. 3 µm). This situation of smaller quartz grains within/on carbonaceous walls or sheaths with coarser quartz grains filling the cell lumen is consistent with observations of recent (Campbell et al., 2015) and Proterozoic (Lekele Baghekema et al., 2017; Lepot et al., 2017) microfossils, and of a lenticular specimen from the SPF sample WF4 (Sugitani et al., 2015a). However, this quartz texture is also observed in Type 1 and Type-3 abiotic spheroids. A similar inference of a polysaccharide sheath was made for the quartz ring that encloses a cluster of spheres in the SPF (Schopf, 2006) or clusters of spheres in a Paleoproterozoic formation (Barlow & Van Kranendonk, 2018). Most importantly, the walls of the Type 4 spheroids form closed vesicles in 3D, are wrinkled in all three dimensions, appear partially folded and display flat-lying contacts that resemble appressed, deformed cells (Figure 9). Such features resemble cell-wall deformation that could be caused by growth of appressed living cells, deflation and wrinkling of dead cell walls, or quartz growth deforming walls. Indeed, the observation that single quartz crystals may fill most of a Type 4 spheroid make it possible that the general shape of its outer wall results from crystalline growth. These features are, however, dissimilar to microspherical opal growths (Jones & Renaut, 2007) and cannot be readily explained by coalescence patterns.

Heterogeneity in apparent diameters of the spheroids within the Type 4 cluster is suggested by optical microscopy (Figure 9a) and may be used to argue for abiotic morphogenesis (Schopf, 1976), as observed in opal (Jones & Renaut, 2007) and in organic biomorphs (Fayolle et al., 2017; McMahon & Cosmidis, 2021). However, this heterogeneity is less clear in CLSM 3D imaging. In places, the coalescent outer walls, which may represent capsules of multiple cells, are difficult to distinguish from inner walls (Figure 9a versus 9c). Moreover, such putative deformed cells are expected to generate a wide range of diameters in single focal planes, as observed in recent microfossils (Figure S4D-E in (Lepot et al., 2014). We, thus, suggest that the apparent diameter heterogeneity within this cluster may be explained by the cross-sectional effect, deformation, or association of multiple species in addition to abiotic morphogenesis.

## 5.7 | Pustules and depressions on Type 5 spheroids

The large Type 5 spheroid displays multiple pustules along its outer boundary (Figures 11 and 12) that contrast with the inner vesicles documented in large spherical microstructures of the Farrel Quartzite (Sugitani, 2009a). So far, we are unable to relate these wall-linked pustules with known cellular ultrastructures. They are infilled with organic-poor quartz similar to the central body of the spheroid. To the best of our knowledge, the features of the pustules do not fit with a potential cellular division pattern or budding (Ferrario, Guerrero, & Alzamora, 2014), due to the spacing between each vesicle (Figures 11a versus 11b), integration within the main boundary of the sphere, and protrusion in and out of the main sphere. Moreover, a localized crystal growth encapsulated within carbonaceous walls may displace the organic matter and locally reduce/increase its thickness and/or pierce it as observed in microfossils of the Gunflint Formation (Lepot et al., 2017). We note, that in this case the organic matter may represent primary kerogen (Alleon et al., 2016; Lepot et al., 2017) or migrated oil (Rasmussen et al., 2021).

Interestingly, the pustules in the wall of the Type 5 spheroid are coated by organic matter on both sides of the wall. In contrast, the pustule formed by growth of pyrite along the outer wall of a Type 2 spheroid (Figure 7) is only coated by carbonaceous matter on its outer side. In addition, the pustules form a thin wall on either the outer (double green arrow, Figure 11) or inner side (yellow arrows, Figure 11) opposite to the thicker part of the main wall. The thicker part of the main wall and the thinner opposite wall of pustules are of constant thicknesses. Collectively this argues that the shape of the pustules is not linked with recrystallization of quartz. The pustules may have formed through a taphonomic process, abiogenic templating by early silica precipitates, or a combination of both.

Furthermore, the carbonaceous matter of the pustules is essentially located at grain boundaries, in particular along the thicker, main wall, and is only embedded as nanoparticulate section in the thinner part. Arcuate series of crystal boundaries are observed not only along the main wall, the thin pustule walls but also along non-carbonaceous crystal boundaries within the Type-5 spheroid. Depressions in the main wall appear to be linked with siliceous spheroids that are only carbonaceous in contact with the spheroid wall (green arrows in Figure 12). As such, these depressions may have formed through displacement of carbonaceous matter during growth of siliceous spheroids, which is consistent with a taphonomic process. Alternatively, it remains difficult to rule out the possibility that the Type 5 spheroids formed by coalescence of multiple silica (hemi)spheres associated with bitumen coating.

## 5.8 | Organic biomorph hypothesis

The formation of organic-sulfur biomorphs (Cosmidis, Nims, Diercks, & Templeton, 2019; Cosmidis & Templeton, 2016) appears plausible in the SPF due to the presence of sulfidic conditions, likely hydrothermal, that precipitated sulfides. Sphere coalescence patterns and internal vesicles of Types-1-3 spheroids can all be explained by abiotic self-assembly of organic biomorphs (McMahon & Cosmidis, 2021). Organic-sulfur biomorphs have been shown to preserve during early silica encrustation experiments (Nims et al., 2021), as have proteinoid spheroids (Fox & Yuyama, 1963; Francis, Margulis, & Barghoorn, 1978). However, we do not know whether the shape of abiotic organic spheroids could be preserved during advanced quartz (re)crystallization and metamorphism, which should be tested with further experiments. Moreover, the internal carbonaceous masses observed in Type 1 spheroids, and to a lesser extent in Types 2–3 spheroids are difficult to reconcile with organic microstructures shaped abiotically that can either form dense organic spheres (non-cellular, e.g., (Criouet, Viennet, Jacquemot, Jaber, & Bernard, 2021) or cellular biomorphs with vesicular inclusions (McMahon & Cosmidis, 2021). The vesicular inclusions in cellular biomorphs do not appear to display enough organic matter to form the dense internal masses in Type 1 spheroids. Although we cannot completely rule out silicification of organic biomorphs, the observed textures in Types 1–3 spheroids appear best reconciled with morphogenesis associated with carbonaceous matter migration in or onto a silica substrate.

## 6 | CONCLUSION

This extensive study of five new types of spherical microstructures in ~3.4 Ga chert of the SPF yielded new textural features as well as silica–carbon relationships (Table 1). Type 1–3 spheroids revealed some similarities with *Leptoteichos golubicii* and *Huronispora*, genuine fossils of the Paleoproterozoic, and with chroococcalean cyanobacteria from Neoproterozoic and younger strata. However, we find that coalescence patterns that form clusters of multiple hemispheres with single (Type 1) or multiple (Type 3) walls, are best interpreted as the coatings of abiotic siliceous templates (such as botryoids) by ambient organic matter, or Liesegang rings formed by carbonaceous matter diffusion in a gel or poorly-crystalline silica phase. The morphogenesis of coalescent spheroids of silica and pyrite may have been influenced by such ambient organic matter. The non-coalescent members of Type 1 and Type 3 spheroids thus most plausibly formed in a similar fashion, thus mimicking microfossils (e.g., Figure 8c). The fact that carbonaceous walls in Type 1 and Type-3 spheroids and internal spheroids in Type 2 microstructures are dominated by nanoparticulate textures partly embedded in multi-micrometric quartz crystals is consistent with migrated organic matter, possibly originating in their internal carbonaceous masses. Nevertheless, we lack observations on genuine silicified microfossils in rocks with a similar metamorphic grade that might also reveal inclusion of nanoparticulate cellular walls in coarse quartz. The nanoparticulate nature of these walls makes it unlikely that such spheroids can be preserved after acid dissolution of the quartz matrix.

In contrast with Type 1 and Type 3 spheroids, Type 2 spheroids display a sub-continuous outer wall lying at quartz crystal boundaries. Type 2 spheroids do not display coalescence of their outer walls, which may, thus, be cellular in origin. Internal vesicles within Type 2 spheroids are multiple and coalescent, which is likely an abiogenic feature that may have formed inside a putative microfossil. Moreover, sub-continuous carbonaceous walls were also observed on coalescent internal vesicles, which raises question about the use of this textural feature in general as a criterion to identify microfossils in chert. As such Type 2 spheroids remain dubiofossils with abiotic internal vesicles.

Type 4 spheroids exhibit some additional features including sub-continuous bi-layered walls with shapes suggestive of cell deformation, colony-like association that may have formed with polysaccharide envelope. Clustered spheroids identified within the SPF rocks (e.g., Figures 4m-n in Schopf, 2006) have been interpreted as chroococcacean cyanobacterium-like organisms. The latter displayed highly granular single walls and appeared encapsulated in a common capsule. Tightly clustered and apparently deformed cell-like structures have been observed in a Paleoproterozoic microfossil assemblage (e.g., Figure 7e in Barlow & Van Kranendonk, 2018). However, the absence of a common capsule and the presence of a second wall (that may represent a polysaccharide capsule), respectively, distinguish the Type 4 spheroids of these other occurrences. Abundant clusters of smaller spheres (~10 μm in diameter) have been observed in the Farrel Quartzite and the SPF (Grey & Sugitani, 2009; Sugitani et al., 2010). These are distinct from our Type 4 cluster in that they are not tightly compressed, they are single-layered and display thick, irregular walls rather than relatively thin and sub-continuous walls. Altogether, Type 4 spheroids appear as plausible candidates for the oldest spheroid microfossils. Due to their scarcity and clustering, these spheroids might be difficult to observe in demineralized samples.

Type 5 consists of a so-far unique, unusually complex spheroid. It displays a thick main wall that appeared highly continuous in CLSM, consistent with cell wall preservation. The pustular structure of the outer wall is difficult to reconcile with abiotic coalescence patterns observed in Types 1–3 spheroids, and pustules grow within the wall in a fashion similar to quartz growths observed in Proterozoic microfossils. The existence of hemispheric depressions in the outer wall also argues for a spherulitic growth that postdates the formation of the outer wall, also consistent with a taphonomic origin. The Type 5 spheroid may thus be considered as a possible microfossil. Its continuous carbonaceous wall lying at grain boundaries may be preserved upon acid maceration but this needs to be tested. Spheres with a size as large as that observed in our Type 5 specimen have been interpreted as possible eukaryotic microorganisms or colonial envelopes of cyanobacteria, or extinct prokaryotes with an unknown metabolism (Javaux et al., 2010). However, these organic-walled spheres (acritarchs) differ from those reported here by their taphonomy as they occur as a large population, they are preserved as hollow folded wrinkled carbonaceous vesicles compressed parallel to bedding in shales and they keep their integrity following acid extraction (Javaux et al., 2010). Auto-assembly of organic molecules may form large vesicles in laboratory experiments (Chen & Walde, 2010; Deamer, 2021; Gözen et al., 2022; McMahon & Cosmidis, 2021) but their preservation in the rock record and taphonomy is unknown and needs to be tested in different preservation windows and lithologies (shale and chert) (Javaux et al., 2010). Another interpretation for large vesicles is giant sulfur bacteria (Czaja, Beukes & Osterhout, 2016), suggested by an association with numerous sulfides (Sugitani et al., 2015b; Figure 1) that could have precipitated in an $H_2S$-rich environment favorable to sulfide oxidation carried out by such bacteria.

In conclusion, most (sub)spherical microstructures co-occurring within the studied samples show morphological gradients and organo-mineral textures that can be explained by abiotic processes, with the exception of the rare colonial-like association of Type 4 spheres with folded winkled appressed walls, and perhaps Type 5 spheres which display some features consistent with the taphonomy of cells. The observation that abiotic objects might co-occur in the same rock with putative microfossils might actually imply an abiotic origin for all objects studied herein within a gradient of abiotic morphogenesis or might reflect the complexity of silicification, especially during the Archean. Future analyses of demineralized specimens might strengthen these interpretations. This study highlights the significance of nanoscale petrology to elucidate the carbonaceous matter-quartz relationships and the discontinuous and particulate nature of spheroid walls that may be mistaken for true microfossils when observed only at micron-scale with light microscopy. Our observations illustrate some of the challenges faced by paleobiologists and astrobiologists looking for unambiguous traces of life in the geological record.

## ACKNOWLEDGMENTS

For SEM analyses and training we thank Philippe Recourt (LOG, U. Lille). We thank the UMS2014/US41 PLBS- BICeL Campus CS Facility for access to instruments and technical advice (CLSM microscopy). Jian Wang (Canadian Light Source) is thanked for help with STXM analyses. The Canadian Light Source is thanked for access to beamline 10ID-1. The Chevreul Institute is thanked for its help in the development of this work through the ARCHI-CM projectsupported by the "Ministère de l'Enseignement Supérieur de la Recherche et de l'Innovation, the region "Hauts-de-France," the ERDF program of the European Union and the "Métropole Européenne de Lille." FIB work was partly supported by the French RENATECH network.

## DATA AVAILABILITY STATEMENT

The data that support the findings of this study are available from the corresponding author upon reasonable request.

## ORCID

*Maxime Coutant* https://orcid.org/0000-0002-3185-2156
*Alexandre Fadel* https://orcid.org/0000-0001-7282-8649
*Elodie Richard* https://orcid.org/0000-0003-0438-4024
*Kenichiro Sugitani* https://orcid.org/0000-0002-8668-5658

## REFERENCES

Alleon, J., Bernard, S., Le Guillou, C., Beyssac, O., Sugitani, K., & Robert, F. (2018). Chemical nature of the 3.4 Ga Strelley Pool microfossils. *Geochemical Perspective Letters*, *7*, 37–42. https://doi.org/10.7185/geochemlet.1817

Alleon, J., Bernard, S., le Guillou, C., Marin-Carbonne, J., Pont, S., Beyssac, O., McKeegan, K., & Robert, F. (2016). Molecular preservation of 1.88 Ga Gunflint organic microfossils as a function of temperature and mineralogy. *Nature Communications*, *7*(1), 11977. https://doi.org/10.1038/ncomms11977

Allwood, A. C., Walter, M. R., Kamber, B. S., Marshall, C. P., & Burch, I. W. (2006). Stromatolite reef from the early Archaean era of Australia. *Nature*, *441*(7094), 714–718. https://doi.org/10.1038/nature04764

Barlow, E. V., & Van Kranendonk, M. J. (2018). Snapshot of an early Paleoproterozoic ecosystem: Two diverse microfossil communities from the Turee Creek group, Western Australia. *Geobiology*, *16*(5), 1–27. https://doi.org/10.1111/gbi.12304

Bernard, S., & Horsfield, B. (2014). Thermal maturation of gas shale systems. *Annual Review of Earth and Planetary Sciences*, *42*, 635–651. https://doi.org/10.1146/annurev-earth-060313-054850

Beveridge, T. J., Meloche, J. D., Fyfe, W. S., & Murray, R. G. E. (1983). Diagenesis of metals chemically complexed to bacteria: Laboratory formation of metal phosphates, sulfides, and organic condensates in artificial sediments. *Applied and Environmental Microbiology*, *45*(3), 1094–1108. https://doi.org/10.1128/aem.45.3.1094-1108.1983

Brasier, M. D., Antcliffe, J., Saunders, M., & Wacey, D. (2015). Changing the picture of Earth's earliest fossils (3.5–1.9 Ga) with new approaches and new discoveries. *Proceedings of the National Academy of Sciences*, *112*(16), 4859–4864. https://doi.org/10.1073/pnas.1405338111

Brasier, M. D., Green, O. R., Jephcoat, A. P., Kleppe, A. K., Van Kranendonk, M. J., Lindsay, J. F., Steele, A., & Grassineau, N. V. (2002). Questioning the evidence for Earth's oldest fossils. *Nature*, *416*(6876), 76–81. https://doi.org/10.1038/416076a

Brasier, M. D., Green, O. R., Lindsay, J. F., Mcloughlin, N., Steele, A., & Stoakes, C. A. (2005). Critical testing of Earth's oldest putative fossil assemblage from the ~3.5Ga apex chert, Chinaman Creek, Western Australia. *Precambrian Research*, *140*(1–2), 55–102. https://doi.org/10.1016/j.precamres.2005.06.008

Buick, R. (1990). Microfossil recognition in Archean rocks: An appraisal of spheroids and filaments from a 3500 M.Y. old chert-barite unit at north pole, Western Australia. *PALAIOS*, *5*(5), 441. https://doi.org/10.2307/3514837

Campbell, K. A., Lynne, B. Y., Handley, K. M., Jordan, S., Farmer, J. D., Guido, D. M., Foucher, F., Turner, S., & Perry, R. S. (2015). Tracing biosignature preservation of geothermally silicified microbial textures into the geological record. *Astrobiology*, *15*(10), 858–882. https://doi.org/10.1089/ast.2015.1307

Chen, I. A., & Walde, P. (2010). From self-assembled vesicles to protocells. *Cold Spring Harbor Perspectives in Biology*, *2*(7), 1–13. https://doi.org/10.1101/cshperspect.a002170

Cosmidis, J., Nims, C. W., Diercks, D., & Templeton, A. S. (2019). Formation and stabilization of elemental sulfur through organomineralization. *Geochimica et Cosmochimica Acta*, *247*, 59–82. https://doi.org/10.1016/j.gca.2018.12.025

Cosmidis, J., & Templeton, A. S. (2016). Self-assembly of biomorphic carbon/sulfur microstructures in sulfidic environments. *Nature Communications*, *7*, 1–9. https://doi.org/10.1038/ncomms12812

Criouet, I., Viennet, J. C., Jacquemot, P., Jaber, M., & Bernard, S. (2021). Abiotic formation of organic biomorphs under diagenetic conditions. *Geochemical Perspectives Letters*, *16*, 40–46. https://doi.org/10.7185/GEOCHEMLET.2102

Czaja, A. D., Beukes, N. J., & Osterhout, J. T. (2016). Sulfur-oxidizing bacteria prior to the Great Oxidation Event from the 2.52 Ga Gamohaan Formation of South Africa. *Geology*, *44*(12), 983–986. https://doi.org/10.1130/g38150.1

Deamer, D. (2021). Where did life begin? Testing ideas in prebiotic analogue conditions. *Life*, *11*(2), 1–11. https://doi.org/10.3390/life11020134

Delarue, F., Robert, F., Derenne, S., Tartèse, R., Jauvion, C., Bernard, S., Pont, S., Gonzalez-Cano, A., Duhamel, R., Sugitani, K., & Sugitani, K. (2020). Out of rock: A new look at the morphological and geochemical preservation of microfossils from the 3.46 Gyr-old Strelley Pool Formation. *Precambrian Research*, *336*(March 2019), 105472. https://doi.org/10.1016/j.precamres.2019.105472

Engel, A. E. J., Nagy, B., Nagy, L. A., Engel, C., Kremp, G. O. W., & Drew, C. M. (1968). Alga-like forms in onverwacht series, South Africa. *Science*, *161*, 1005–1008.

Fadel, A., Lepot, K., Busigny, V., Addad, A., & Troadec, D. (2017). Iron mineralization and taphonomy of microfossils of the 2.45–2.21 Ga Turee Creek group, Western Australia. *Precambrian Research*, *298*, 530–551. https://doi.org/10.1016/j.precamres.2017.07.003

Fayolle, D., Altamura, E., D'Onofrio, A., Madanamothoo, W., Fenet, B., Mavelli, F., Buchet, R., Stano, P., Fiore, M., & Strazewski, P. (2017). Crude phosphorylation mixtures containing racemic lipid amphiphiles self-assemble to give stable primitive compartments. *Scientific Reports*, *7*(1), 1–11. https://doi.org/10.1038/s41598-017-18053-y

Ferrario, M., Guerrero, S., & Alzamora, S. M. (2014). Study of pulsed light-induced damage on Saccharomyces cerevisiae in apple juice by flow cytometry and transmission electron microscopy. *Food and*

*Bioprocess Technology*, *7*(4), 1001–1011. https://doi.org/10.1007/s11947-013-1121-9

Fontboté, L., Kouzmanov, K., Chiaradia, M., & Pokrovski, G. S. (2017). Sulfide minerals in hydrothermal deposits. *Elements*, *13*(2), 97–103. https://doi.org/10.2113/gselements.13.2.97

Fox, S. W., & Yuyama, S. (1963). Abiotic production of Primite protein and formed microparticles. *Annals New York Academy of Sciences*, *3971*(5), 487–495.

Francis, S., Margulis, L., & Barghoorn, E. S. (1978). On the experimental silicification of microorganisms II. On the time of appearance of eukaryotic organisms in the fossil record. *Precambrian Research*, *6*(1), 65–100. https://doi.org/10.1016/0301-9268(78)90055-4

Gao, S., Huang, F., Wang, Y., & Gao, W. (2016). A review of research Progress in the genesis of colloform pyrite and its environmental indications. *Acta Geologica Sinica - English Edition*, *90*(4), 1353–1369. https://doi.org/10.1111/1755-6724.12774

Glikson, M., Duck, L. J., Golding, S. D., Hofmann, A., Bolhar, R., Webb, R., Baiano, J. C. F., & Sly, L. I. (2008). Microbial remains in some earliest earth rocks: Comparison with a potential modern analogue. *Precambrian Research*, *164*(3–4), 187–200. https://doi.org/10.1016/j.precamres.2008.05.002

Gong, J., Myers, K. D., Munoz-Saez, C., Homann, M., Rouillard, J., Wirth, R., Schreiber, A., & van Zuilen, M. (2020). Formation and preservation of microbial palisade fabric in silica deposits from El Tatio, Chile. *Astrobiology*, *20*(4), 500–524. https://doi.org/10.1089/ast.2019.2025

Gözen, I., Köksal, E. S., Põldsalu, I., Xue, L., Spustova, K., Pedrueza-Villalmanzo, E., Ryskulov, R., Meng, F., & Jesorka, A. (2022). Protocells: Milestones and recent advances. *Small*, *2106624*, 2106624. https://doi.org/10.1002/smll.202106624

Grey, K., & Sugitani, K. (2009). Palynology of Archean microfossils (c. 3.0Ga) from the Mount Grant area, Pilbara craton, Western Australia: Further evidence of biogenicity. *Precambrian Research*, *173*(1–4), 60–69. https://doi.org/10.1016/j.precamres.2009.02.003

Grey, K., & Willman, S. (2009). Taphonomy of Ediacaran acritarchs from Australia: Significance for taxonomy and biostratigraphy. *PALAIOS*, *24*(4), 239–256. https://doi.org/10.2110/palo.2008.p08-020r

Hickman-Lewis, K., Cavalazzi, B., Foucher, F., & Westall, F. (2018). Most ancient evidence for life in the Barberton greenstone belt: Microbial mats and biofabrics of the ~3.47 Ga middle marker horizon. *Precambrian Research*, *312*(October 2017), 45–67. https://doi.org/10.1016/j.precamres.2018.04.007

Hickman-Lewis, K., Garwood, R. J., Brasier, M. D., Goral, T., Jiang, H., McLoughlin, N., & Wacey, D. (2016). Carbonaceous microstructures from sedimentary laminated chert within the 3.46 Ga apex basalt, Chinaman Creek locality, Pilbara, Western Australia. *Precambrian Research*, *278*, 161–178. https://doi.org/10.1016/j.precamres.2016.03.013

House, C. H., Oehler, D. Z., Sugitani, K., & Mimura, K. (2013). Carbon isotopic analyses of ca. 3.0 Ga microstructures imply planktonic autotrophs inhabited Earth's early oceans. *Geology*, *41*(6), 651–654. https://doi.org/10.1130/G34055.1

Javaux, E. J. (2019). Challenges in evidencing the earliest traces of life. *Nature*, *572*(7770), 451–460. https://doi.org/10.1038/s41586-019-1436-4

Javaux, E. J., & Lepot, K. (2018). The Paleoproterozoic fossil record: Implications for the evolution of the biosphere during Earth's middle-age. *Earth-Science Reviews*, *176*(October 2017), 68–86. https://doi.org/10.1016/j.earscirev.2017.10.001

Javaux, E. J., Marshall, C. P., & Bekker, A. (2010). Organic-walled microfossils in 3.2-billion-year-old shallow-marine siliciclastic deposits. *Nature*, *463*(7283), 934–938. https://doi.org/10.1038/nature08793

Jones, B., & Renaut, R. W. (2007). Microstructural changes accompanying the opal-a to opal-CT transition: New evidence from the siliceous sinters of Geysir, Haukadalur, Iceland. *Sedimentology*, *54*(4), 921–948. https://doi.org/10.1111/j.1365-3091.2007.00866.x

Kile, D. (2002). Occurrence and genesis of thunder eggs containing plume and Moss agate. *Rocks & Minerals*, *77*(4), 252–268. https://doi.org/10.1080/00357529.2002.9925643

Kim-Zajonz, J., Werner, S., & Schulz, H. (1999). High pressure single crystal X-ray diffraction study on α -quartz. *Zeitschrift Für Kristallographie - Crystalline Materials*, *214*(6), 324–330. https://doi.org/10.1524/zkri.1999.214.6.324

Knoll, A. H., Barghoorn, E. S., & Awramik, S. M. (1978). New microorganisms from the Aphebian gunflint iron formation, Ontario. *Journal of Paleontology*, *52*(5), 976–992.

Knoll, A. H., Strother, P. K., & Rossi, S. (1988). Distribution and diagenesis of microfossils from the lower proterozoic duck creek dolomite, Western Australia. *Precambrian Research*, *38*(3), 257–279. https://doi.org/10.1016/0301-9268(88)90005-8

Lekele Baghekema, S. G., Lepot, K., Riboulleau, A., Fadel, A., Trentesaux, A., & El Albani, A. (2017). Nanoscale analysis of preservation of ca. 2.1 Ga old Francevillian microfossils, Gabon. *Precambrian Research*, *301*(August), 1–18. https://doi.org/10.1016/j.precamres.2017.08.024

Lepot, K. (2020). Signatures of early microbial life from the Archean (4 to 2.5 Ga) eon. *Earth-Science Reviews*, *209*, 103296. https://doi.org/10.1016/j.earscirev.2020.103296

Lepot, K., Addad, A., Knoll, A. H., Wang, J., Troadec, D., Béché, A., & Javaux, E. J. (2017). Iron minerals within specific microfossil morphospecies of the 1.88 Ga gunflint formation. *Nature Communications*, *8*(1), 14890. https://doi.org/10.1038/ncomms14890

Lepot, K., Compère, P., Gérard, E., Namsaraev, Z., Verleyen, E., Tavernier, I., Hodgson, D. A., Vyverman, W., Gilbert, B., Wilmotte, A., & Javaux, E. J. (2014). Organic and mineral imprints in fossil photosynthetic mats of an East Antarctic lake. *Geobiology*, *12*(5), 424–450. https://doi.org/10.1111/gbi.12096

Lepot, K., Williford, K. H., Ushikubo, T., Sugitani, K., Mimura, K., Spicuzza, M. J., & Valley, J. W. (2013). Texture-specific isotopic compositions in 3.4Gyr old organic matter support selective preservation in cell-like structures. *Geochimica et Cosmochimica Acta*, *112*, 66–86. https://doi.org/10.1016/j.gca.2013.03.004

Marshall, C. P., Love, G. D., Snape, C. E., Hill, A. C., Allwood, A. C., Walter, M. R., Van Kranendonk, M. J., Bowden, S. A., Sylva, S. P., & Summons, R. E. (2007). Structural characterization of kerogen in 3.4Ga Archaean cherts from the Pilbara craton, Western Australia. *Precambrian Research*, *155*(1–2), 1–23. https://doi.org/10.1016/j.precamres.2006.12.014

McCollom, T. M., & Seewald, J. S. (2006). Carbon isotope composition of organic compounds produced by abiotic synthesis under hydrothermal conditions. *Earth and Planetary Science Letters*, *243*(1–2), 74–84. https://doi.org/10.1016/j.epsl.2006.01.027

McMahon, S., & Cosmidis, J. (2021). False biosignatures on Mars: Anticipating ambiguity. *Journal of the Geological Society*, *179*, jgs2021-050. https://doi.org/10.1144/jgs2021-050

Mendelson, C. V., & Schopf, J. W. (1992). Proterozoic and selected early Cambrian microfossils and microfossil-like objects. In *The Proterozoic biosphere* (pp. 865–952). Cambridge University Press. https://doi.org/10.1017/CBO9780511601064.024

Merinero, R., Cárdenes, V., Lunar, R., Boone, M. N., & Cnudde, V. (2017). Representative size distributions of framboidal, euhedral, and sunflower pyrite from high-resolution X-ray tomography and scanning electron microscopy analyses. *American Mineralogist*, *102*(3), 620–631. https://doi.org/10.2138/am-2017-5851

Nagy, B., & Nagy, L. A. (1969). Early pre-Cambrian Onverwacht microstructures: Possibly the oldest fossils on earth? *Nature*, *223*(5212), 1226–1229. https://doi.org/10.1038/2231226a0

Nims, C., Lafond, J., Alleon, J., Templeton, A. S., & Cosmidis, J. (2021). Organic biomorphs may be better preserved than microorganisms in early earth sediments. *Geology*, *49*(6), 629–634. https://doi.org/10.1130/G48152.1

Oehler, J. H. (1976). Experimental studies in Precambrian paleontology: Structural and chemical changes in blue-green algae during simulated fossilization in synthetic chert. *Geological Society of America Bulletin*, *87*(1), 117. https://doi.org/10.1130/0016-7606(1976)87<117:ESIPPS>2.0.CO;2

Oehler, D. Z., Robert, F., Walter, M. R., Sugitani, K., Meibom, A., Mostefaoui, S., & Gibson, E. K. (2010). Diversity in the Archean biosphere: New insights from NanoSIMS. *Astrobiology*, *10*(4), 413–424. https://doi.org/10.1089/ast.2009.0426

Oehler, D. Z., Walsh, M. M., Sugitani, K., Liu, M., & House, C. H. (2017). Large and robust lenticular microorganisms on the young earth. *Precambrian Research*, *296*, 112–119. https://doi.org/10.1016/j.precamres.2017.04.031

Pang, K., Tang, Q., Schiffbauer, J. D., Yao, J., Yuan, X., Wan, B., Chen, L., Ou, Z., & Xiao, S. (2013). The nature and origin of nucleus-like intracellular inclusions in Paleoproterozoic eukaryote microfossils. *Geobiology*, *11*(6), 499–510. https://doi.org/10.1111/gbi.12053

Papineau, D., She, Z., & Dodd, M. S. (2017). Chemically-oscillating reactions during the diagenetic oxidation of organic matter and in the formation of granules in late Palaeoproterozoic chert from Lake Superior. *Chemical Geology*, *470*(August), 33–54. https://doi.org/10.1016/j.chemgeo.2017.08.021

Pflug, H. D. (1967). Structured organic remains from the fig tree series (Precambrian) of the Barberton mountain land (South Africa). *Review of Palaeobotany and Palynology*, *5*(1–4), 9–29. https://doi.org/10.1016/0034-6667(67)90205-9

Rasmussen, B., Muhling, J. R., & Fischer, W. W. (2021). Ancient oil as a source of carbonaceous matter in 1.88-billion-year-old gunflint stromatolites and microfossils. *Astrobiology*, *21*(9), 655–672. https://doi.org/10.1089/ast.2020.2376

Rouillard, J., Van Zuilen, M., Pisapia, C., & Garcia-Ruiz, J. M. (2021). An alternative approach for assessing biogenicity. *Astrobiology*, *21*(2), 151–164. https://doi.org/10.1089/ast.2020.2282

Schopf, J. W. (1976). Are the oldest? Fossils?, fossils? *Origins of Life*, *7*(1), 19–36. https://doi.org/10.1007/BF01218511

Schopf, J. W. (2006). Fossil evidence of Archaean life. *Philosophical Transactions of the Royal Society B: Biological Sciences*, *361*(1470), 869–885. https://doi.org/10.1098/rstb.2006.1834

Schopf, J. W., Kudryavtsev, A. B., Osterhout, J. T., Williford, K. H., Kitajima, K., Valley, J. W., & Sugitani, K. (2017). An anaerobic ~3400 ma shallow-water microbial consortium: Presumptive evidence of Earth's Paleoarchean anoxic atmosphere. *Precambrian Research*, *299*(March), 309–318. https://doi.org/10.1016/j.precamres.2017.07.021

Schopf, J. W., Tripathi, A. B., & Kudryavtsev, A. B. (2006). Three-dimensional confocal optical imagery of Precambrian microscopic organisms. *Astrobiology*, *6*(1), 1–16. https://doi.org/10.1089/ast.2006.6.1

Stanier, R. Y., Kunisawa, R., Mandel, M., & Cohen-Bazire, G. (1971). Purification and properties of unicellular blue-green algae (order Chroococcales). *Bacteriological Reviews*, *35*(2), 171–205. https://doi.org/10.1128/MMBR.35.2.171-205.1971

Sugitani, K., Grey, K., Allwood, A. C., Nagaoka, T., Mimura, K., Minami, M., Marshall, C. P., Van Kranendonk, M. J., & Walter, M. R. (2007). Diverse microstructures from Archaean chert from the mount Goldsworthy-Mount Grant area, Pilbara craton, Western Australia: Microfossils, dubiofossils, or pseudofossils? *Precambrian Research*, *158*(3–4), 228–262. https://doi.org/10.1016/j.precamres.2007.03.006

Sugitani, K., Grey, K., Nagaoka, T., & Mimura, K. (2009). Three-dimensional morphological and textural complexity of Archean putative microfossils from the northeastern Pilbara craton: Indications of biogenicity of large (>15 μm) spheroidal and spindle-like structures. *Astrobiology*, *9*(7), 603–615. https://doi.org/10.1089/ast.2008.0268

Sugitani, K., Grey, K., Nagaoka, T., Mimura, K., & Walter, M. R. (2009). Taxonomy and biogenicity of Archaean spheroidal microfossils (ca. 3.0 Ga) from the mount Goldsworthy-Mount Grant area in the northeastern Pilbara craton, Western Australia. *Precambrian Research*, *173*(1–4), 50–59. https://doi.org/10.1016/j.precamres.2009.02.004

Sugitani, K., Lepot, K., Nagaoka, T., Mimura, K., Van Kranendonk, M. J., Oehler, D. Z., & Walter, M. R. (2010). Biogenicity of morphologically diverse carbonaceous microstructures from the ca. 3400 Ma Strelley Pool formation, in the Pilbara craton, Western Australia. *Astrobiology*, *10*(9), 899–920. https://doi.org/10.1089/ast.2010.0513

Sugitani, K., Mimura, K., Nagaoka, T., Lepot, K., & Takeuchi, M. (2013). Microfossil assemblage from the 3400 Ma Strelley Pool formation in the Pilbara craton, Western Australia: Results form a new locality. *Precambrian Research*, *226*, 59–74. https://doi.org/10.1016/j.precamres.2012.11.005

Sugitani, K., Mimura, K., Takeuchi, M., Lepot, K., Ito, S., & Javaux, E. J. (2015). Early evolution of large micro-organisms with cytological complexity revealed by microanalyses of 3.4 Ga organic-walled microfossils. *Geobiology*, *13*(6), 507–521. https://doi.org/10.1111/gbi.12148

Sugitani, K., Mimura, K., Takeuchi, M., Yamaguchi, T., Suzuki, K., Senda, R., Asahara, Y., Wallis, S., & Van Kranendonk, M. J. (2015). A Paleoarchean coastal hydrothermal field inhabited by diverse microbial communities: The Strelley Pool formation, Pilbara craton, Western Australia. *Geobiology*, *13*(6), 522–545. https://doi.org/10.1111/gbi.12150

Tyler, S. A., & Barghoorn, E. S. (1954). Occurrence of structurally preserved plants in pre-Cambrian rocks of the Canadian shield. *Science*, *119*(3096), 606–608. https://doi.org/10.1126/science.119.3096.606

Ueno, Y., Isozaki, Y., & McNamara, K. J. (2006). Coccoid-like microstructures in a 3.0 Ga chert from Western Australia. *International Geology Review*, *48*(1), 78–88. https://doi.org/10.2747/0020-6814.48.1.78

Van Kranendonk, M. J. (2006). Volcanic degassing, hydrothermal circulation and the flourishing of early life on earth: A review of the evidence from c. 3490–3240 Ma rocks of the Pilbara supergroup, Pilbara craton, Western Australia. *Earth-Science Reviews*, *74*(3–4), 197–240. https://doi.org/10.1016/j.earscirev.2005.09.005

Wacey, D., Kilburn, M. R., Saunders, M., Cliff, J., & Brasier, M. D. (2011). Microfossils of Sulphur-metabolizing cells in 3.4-billion-year-old rocks of Western Australia. *Nature Geoscience*, *4*(10), 698–702. https://doi.org/10.1038/ngeo1238

Wacey, D., Menon, S., Green, L., Gerstmann, D., Kong, C., Mcloughlin, N., Saunders, M., & Brasier, M. D. (2012). Taphonomy of very ancient microfossils from the ~3400 Ma Strelley Pool formation and ~1900 Ma gunflint formation: New insights using a focused ion beam. *Precambrian Research*, *220–221*, 234–250. https://doi.org/10.1016/j.precamres.2012.08.005

Wacey, D., Noffke, N., Saunders, M., Guagliardo, P., & Pyle, D. M. (2018). Volcanogenic pseudo-fossils from the ~3.48 Ga dresser formation, Pilbara, Western Australia. *Astrobiology*, *18*(5), 539–555. https://doi.org/10.1089/ast.2017.1734

Wacey, D., Saunders, M., & Kong, C. (2018). Remarkably preserved tephra from the 3430 Ma Strelley Pool formation, Western Australia: Implications for the interpretation of Precambrian microfossils. *Earth and Planetary Science Letters*, *487*, 33–43. https://doi.org/10.1016/j.epsl.2018.01.021

Walsh, M. M. (1992). Microfossils and possible microfossils from the early archean Onverwacht group, Barberton mountain land, South Africa. *Precambrian Research*, *54*(2–4), 271–293. https://doi.org/10.1016/0301-9268(92)90074-X

Westall, F., & Folk, R. L. (2003). Exogenous carbonaceous microstructures in early Archaean cherts and BIFs from the Isua Greenstone Belt: Implications for the search for life in ancient rocks. *Precambrian Research*, *126*(3–4), 313–330. https://doi.org/10.1016/S0301-9268(03)00102-5

Yoshida, H., Kuma, R., Hasegawa, H., Katsuta, N., Sirono, S.-I., Minami, M., Nishimoto, S., Takagi, N., Kadowaki, S., & Metcalfe, R. (2021). Syngenetic rapid growth of ellipsoidal silica concretions with bitumen cores. *Scientific Reports*, *11*(1), 1–11. https://doi.org/10.1038/s41598-021-83651-w

## SUPPORTING INFORMATION

Additional supporting information may be found in the online version of the article at the publisher's website.

**How to cite this article:** Coutant, M., Lepot, K., Fadel, A., Addad, A., Richard, E., Troadec, D., Ventalon, S., Sugitani, K., & Javaux, E. J. (2022). Distinguishing cellular from abiotic spheroidal microstructures in the ca. 3.4 Ga Strelley Pool Formation. *Geobiology*, *00*, 1–24. https://doi.org/10.1111/gbi.12506